

A conservative, discontinuous Galerkin, tracer transport scheme using compatible finite elements

Timothy C. Andrews ^{*1,2} and Thomas M. Bendall³

¹Department of Mathematics and Statistics, University of Exeter, Exeter, United Kingdom

²Department of Climate and Space Sciences and Engineering, University of Michigan, Ann Arbor, MI, USA

³Dynamics Research, Met Office, Exeter, United Kingdom

March 20, 2026

Abstract

This paper outlines a conservative transport scheme for scalar tracers within a compatible finite element model for geophysical fluid equations. Instead of using the advective transport equation for a mixing ratio, a conservative transport equation is solved for the tracer density of the mixing ratio multiplied by the dry density. This ensures mass conservation in the continuous equations, which can be preserved in the discrete equations with a discontinuous Galerkin transport scheme. Our method is designed to work for two placements of the mixing ratio in a Charney-Phillips vertical staggering: either co-located with the dry density or vertically staggered from it. The new scheme is designed to conserve the tracer density and ensure consistency by maintaining a constant mixing ratio. Additionally, a mass-conserving limiter is developed to ensure non-negativity in the co-located configuration. Tests with terminator toy chemistry and a moist rising bubble show the use of the new transport scheme with physics terms and its ability to accurately model mass conservation of moisture species in a dynamical core setup.

1 Introduction

Ensuring mass conservation of dry air and other tracers is one of the key properties of an effective dynamical core for numerical weather prediction and longer climate simulations (Staniforth & Thuburn, 2012; Thuburn, 2008). Accordingly, many design decisions in operational and research dynamical cores, such as the choice of transport scheme, are made with a focus on mass conservation. Some transport schemes are inherently mass-conserving, such as a finite volume discretisation of a flux-form conservative equation. Such a discretisation ensures local mass conservation — that mass lost from one grid cell is transferred to adjacent cells — which implies mass conservation over the entire domain. Methods that are not generally mass-conserving, such as semi-Lagrangian transport, can often be reformulated in a conservative manner, e.g. Zerroukat et al. (2002) and Lauritzen et al. (2010). Other approaches may be globally but not locally mass-conserving, whilst other methods that are not globally conservative typically use mass-fixers to compensate. This work will focus on the discontinuous Galerkin (DG) transport method, which uses a weak form of the governing equations and permits discontinuities between elements. Like the finite volume method, DG discretisations are

*timand@umich.edu

locally, and thus globally, conservative if the continuous equations are conservative. DG methods are commonly used in numerical fluid models as they are inherently parallelisable and well-suited for capturing discontinuous behaviours, such as shocks (Nair et al., 2011).

The transport component of a dynamical core determines the evolution of a field due to advection by winds. Such transported fields include the velocity, potential temperature, pressure, or density of dry air. Additionally, any number of passive or active tracers may also be transported, including aerosols and moisture variables such as water vapour and cloud water fractions. Tracer species are typically defined by a mixing ratio, m , which is the ratio of the *tracer density*, ρ_X , to the density of dry air, ρ :

$$m := \rho_X / \rho. \quad (1)$$

To ensure mass conservation of a species during transport, we require a scheme for the dry air and the mixing ratio such that the globally integrated tracer density remains constant.

There are two types of scalar transport terms that appear in the governing equations used in dynamical cores; these are the *conservative* and *advective* forms. The dry density obeys a conservative transport equation,

$$\frac{\partial \rho}{\partial t} + \nabla \cdot (\rho \mathbf{u}) = 0, \quad (2)$$

with \mathbf{u} the transporting velocity field, whilst mixing ratios are governed by the advective form,

$$\frac{\partial m}{\partial t} + (\mathbf{u} \cdot \nabla) m = 0. \quad (3)$$

Whilst a DG discretisation of the conservative transport equation (2) will be mass-conserving, this is not the case for the advective form (3) as the continuous equation does not conserve mass. To resolve this, we instead consider the time evolution of the tracer density, $\rho_X = \rho m$, using (2) and (3),

$$\frac{\partial}{\partial t}(\rho m) = \frac{\partial \rho}{\partial t} m + \rho \frac{\partial m}{\partial t} = -m \nabla \cdot (\rho \mathbf{u}) - \rho (\mathbf{u} \cdot \nabla) m, \quad (4)$$

which leads to a conservation equation of

$$\frac{\partial}{\partial t}(\rho m) + \nabla \cdot (\rho m \mathbf{u}) = 0. \quad (5)$$

We term (5) a *conservative tracer* transport equation to distinguish it from the conservative transport equation for the dry density (2). Most dynamical cores use the conservative tracer equation in preference to an advective form transport of m , with some models even using tracer densities as prognostic variables in place of mixing ratios, e.g. MPAS (Skamarock et al., 2012) and NICAM (Sato et al., 2008).

Whilst DG methods for conservative tracer transport have been explored previously, such as in Giraldo (1997), Nair et al. (2005), and Bosler et al. (2019), the novelty of this work is that we allow ρ and m to be defined in different function spaces. The use of different function spaces is a key part of the compatible finite element method, which carefully selects spaces that ensure mimetic properties, specifically that the discretisation obeys $\text{curl}(\text{grad}) = \mathbf{0}$ and $\text{div}(\text{curl}) = 0$ (Cotter, 2023; Cotter & Shipton, 2012; Natale et al., 2016). GungHo, the dynamical core for the next-generation LFRic-Atmosphere model from the UK Met Office (Adams et al., 2019; Melvin et al., 2019, 2024) uses a compatible finite element spatial discretisation. However, GungHo does not solve the transport terms with a finite element method, but instead opts for the flux-form semi-Lagrangian transport scheme, SWIFT (Bendall & Kent, 2025).

GungHo uses a Charney-Phillips vertical staggering (Melvin et al., 2018), which offsets the dry density from the thermodynamic variables such as the potential temperature; this avoids the computational mode of the Lorenz grid, where the density and thermodynamic variables are instead co-located in the vertical coordinate. The Charney-Phillips configuration offers a choice of mixing ratio placement: m could either be co-located with the dry density or co-located with the thermodynamic variables, with the latter choice meaning that ρ and m are vertically staggered. Given that

there are advantages to either placement of m (Bendall et al., 2023), our scheme is designed to work in both instances. To ensure mass conservation when ρ and m lie in different function spaces, we require specific operators to map between spaces. Galerkin projections are used to move the density and mixing ratios from their original spaces to a shared transport space. As projecting the mixing ratio in isolation will violate mass conservation, we use a conservative Galerkin projection that acts on the tracer density.

We will consider both the lowest-order ($k = 0$) and next-to-lowest-order ($k = 1$) function spaces, with k denoting the finite element order. Lowest-order finite elements are used in GungHo, as this simplifies the coupling of the dynamics to physical parametrisations, enables the use of finite volume and semi-Lagrangian transport, and retains more similarity to the ENDGame dynamical core used by the Unified Model (Wood et al., 2014), the predecessor of LFRic-Atmosphere. However, a $k = 0$ finite element discretisation of the transport terms is only first-order accurate and is highly diffusive; this is a major reason why DG transport is not used in GungHo. To obtain greater accuracy with $k = 0$ spaces, here we use the recovered space method of Bendall et al. (2019). The recovery scheme uses Galerkin projections and averaging to move the lowest-order field into the next-to-lowest-order space for transport, which allows for second-order accuracy. In the case of a vertical staggering between ρ and m , the function space for the mixing ratio is continuous in the vertical dimension, so we use the embedded DG scheme of Cotter and Kuzmin (2016) to map m to a fully discontinuous transport space.

In addition to ensuring mass conservation, the new conservative tracer transport scheme is designed to obey the *consistency* property, which requires that a spatially constant mixing ratio remains constant after transport. This is a desirable property for a transport scheme, as when m is constant, the conservative tracer equation (5) reduces to a scaled conservative equation for density (2). Hence, any variation in the constant mixing ratio over time implies an inconsistent numerical treatment of the conservative equations for ρ_X and ρ (Machenhauer et al., 2009; Zhang et al., 2008). The last key property of our scheme is non-negativity, which is enforced through a limiter. The challenge is applying the limiter such that mass conservation is not violated, and we design a mean mixing ratio limiter to achieve this. Given the complexity of ensuring mass-conserving limiting with partially continuous function spaces, the limiter is currently designed to work with the co-located configuration.

Our conservative tracer transport scheme will be tested on meshes comprised of quadrilateral elements, although the method generalises to other meshes. Tests with a co-located density and mixing ratio will use a spherical domain with a cubed-sphere mesh. Tests with a vertically staggered density and mixing ratio will use a vertical slice domain, with elements constructed as the tensor product of one-dimensional spaces along the horizontal and vertical dimensions. The tests will be performed using the Gusto code library, which is built upon the Firedrake finite element codebase (Ham et al., 2023). Gusto solves geophysical fluid equation sets using compatible finite elements and is designed for rapid prototyping.

The next section will provide important information about the new transport scheme, including the weak form DG discretisations and the operators used to map fields between function spaces. Section 3 tests the conservation and consistency properties of the scheme with co-located spaces, whilst section 4 tests the same properties with a vertical staggering of ρ and m . Section 5 introduces the mean mixing ratio limiter used to enforce non-negativity, and tests this in a simulation with additional physics terms. The last test in section 6 is a dynamical core-like simulation of a moist rising bubble. Concluding remarks are given in section 7.

2 Background

2.1 Function spaces

Throughout this work, we consider four combinations of function spaces for the prognostic density and mixing ratio. These are constructed from discontinuous Lagrange, dQ_k , or continuous Lagrange, Q_k , elements. The discontinuous Lagrange space is spanned by k th-order polynomials. The continuous

Lagrange space is a subset of dQ_k with the additional constraint of \mathcal{C}^0 continuity between elements, which requires nodes on the facets.

The density is always defined on a function space that is discontinuous in both dimensions, either $\mathbb{V}_{\rho,1} := dQ_1 \otimes dQ_1$ or $\mathbb{V}_{\rho,0} := dQ_0 \otimes dQ_0$, where \otimes denotes the tensor product. We also consider thermodynamic function spaces in a Charney-Phillips vertical staggering, which are continuous in the vertical dimension but remain discontinuous in the horizontal dimension, either $\mathbb{V}_{\theta,1} := dQ_1 \otimes Q_2$ or $\mathbb{V}_{\theta,0} := dQ_0 \otimes Q_1$. We will consider both $m \in \mathbb{V}_\rho$, for the co-location of the mixing ratio with the density, and $m \in \mathbb{V}_\theta$, for a vertical staggering of ρ and m . The order of the density and mixing ratio function spaces are always the same. Visualisations of these four function spaces are shown in Figure 1.

Also shown in Figure 1 are two intermediate fields that are used for mapping between function spaces so that ρ and m are transported in the same space. These are the $\tilde{\mathbb{V}}_1 := Q_1 \otimes Q_1$ space, where the tilde denotes continuity in both dimensions, and the $\hat{\mathbb{V}}_\theta := dQ_1 \otimes dQ_2$ space, with the hat denoting that the space is fully discontinuous. These fields are used in the recovery and embedded DG operations that will be discussed later in this section.

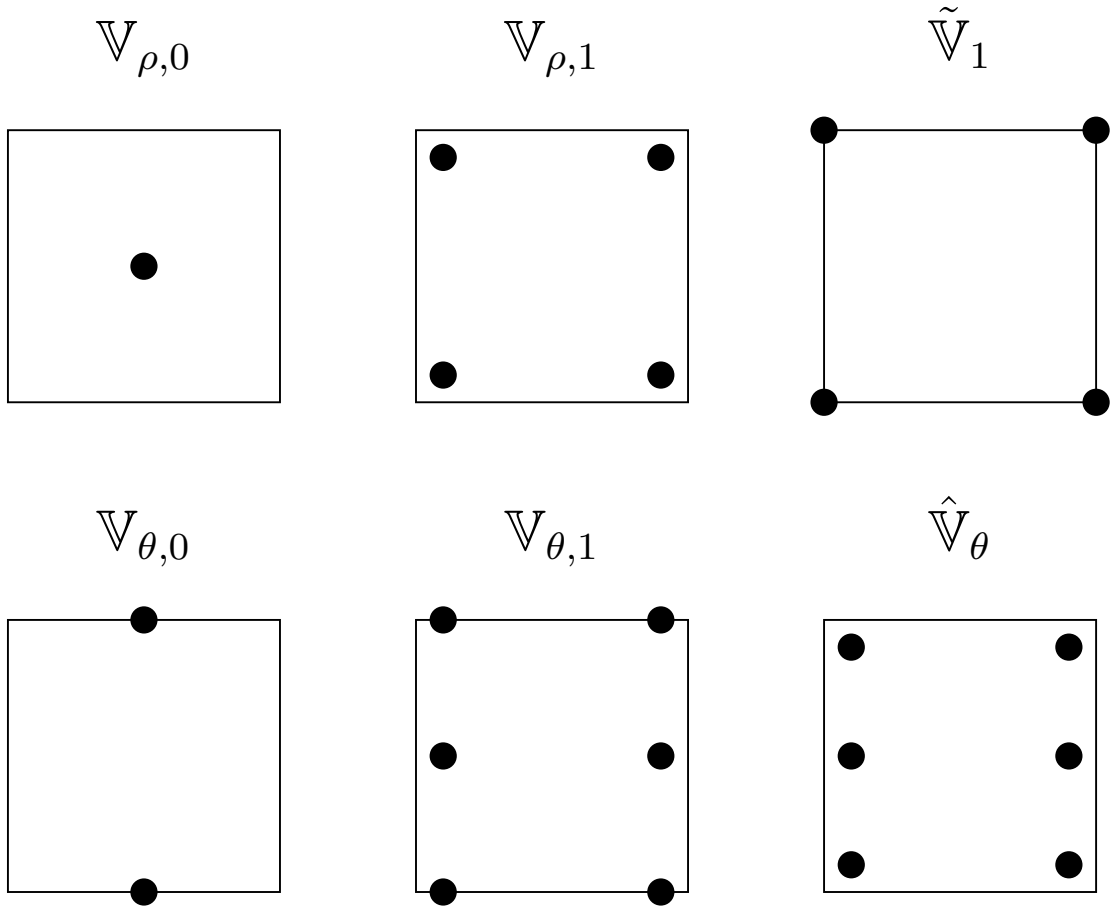


Figure 1: The original function spaces for the density and mixing ratio ($\mathbb{V}_{\rho,0}$, $\mathbb{V}_{\rho,1}$, $\mathbb{V}_{\theta,0}$, $\mathbb{V}_{\theta,1}$), and intermediate spaces used in the recovery and embedded DG operations ($\tilde{\mathbb{V}}_1$, $\hat{\mathbb{V}}_\theta$). Nodes at a facet enforce continuity between adjacent elements.

2.2 Scheme properties

The conservative tracer transport scheme is designed to ensure three key properties:

1. **Conservation:** The total tracer mass should remain unchanged after transport. This can be examined by computing the tracer density of $\rho_X = \rho m$, which should be conserved within the

domain, i.e.

$$\frac{d}{dt} \int_{\Omega} \rho_X \, d\mathbf{x} = 0, \quad (6)$$

where Ω denotes the spatial domain and \mathbf{x} the spatial coordinates. We compute ρ_X as a mean value in each cell by solving

$$\int_{\Omega} \psi \rho_X \, d\mathbf{x} = \int_{\Omega} \psi \rho m \, d\mathbf{x}, \quad \forall \psi \in \mathbb{V}_{\rho,0}, \quad (7)$$

with ρ, m in their original spaces, so they are not necessarily co-located.

The numerical tests will either plot the relative change in tracer density over time,

$$\Delta \rho_X(t) = \frac{|\rho_X(t) - \rho_X(0)|}{\rho_X(0)}, \quad (8)$$

with $|\cdot|$ the absolute value, or compare a mean tracer density error over N time samples,

$$\Delta \rho_X = \frac{1}{N} \sum_{i=1}^N \Delta \rho_X(t_i). \quad (9)$$

2. **Consistency:** A spatially constant mixing ratio remains unchanged over time.
3. **Non-negativity:** Ensuring that the scheme does not introduce any negative mixing ratios, so

$$m(\mathbf{x}) \geq 0, \quad \forall \mathbf{x} \in \Omega. \quad (10)$$

2.3 Mixed Finite Element Formulation

We now overview the mixed finite element equations that describe the transport of the density and mixing ratio. Although ρ and m may live on different function spaces, we ensure that they are represented in a single transport function space, \mathbb{V}_T , before applying the transport operator. In general, this requires an appropriate projection of ρ, m from their original space into the transport space, and then back to their original space after transport.

Consider $\rho, m \in \mathbb{V}_T$, with a conservative transport equation (2) for ρ and a conservative tracer transport equation (5) for m . These equations are multiplied by scalar test functions of $\gamma, \eta \in \mathbb{V}_T$ and integrated over the domain, to obtain the weak forms

$$\int_{\Omega} \gamma \frac{\partial \rho}{\partial t} \, d\mathbf{x} + \int_{\Omega} \gamma \nabla \cdot (\rho \mathbf{u}) \, d\mathbf{x} = 0, \quad \forall \gamma \in \mathbb{V}_T, \quad (11a)$$

$$\int_{\Omega} \eta \frac{\partial (\rho m)}{\partial t} \, d\mathbf{x} + \int_{\Omega} \eta \nabla \cdot (\rho m \mathbf{u}) \, d\mathbf{x} = 0, \quad \forall \eta \in \mathbb{V}_T. \quad (11b)$$

Next, integration by parts is used along with the divergence theorem, which leaves a surface integral term that applies on the set of interior facets, Γ . This surface term is evaluated using discontinuous Galerkin upwinding, leaving

$$\int_{\Omega} \gamma \frac{\partial \rho}{\partial t} \, d\mathbf{x} + \int_{\Gamma} (\mathbf{u}^+ \cdot \hat{\mathbf{n}}^+) \llbracket \gamma \rrbracket_+ \rho^\dagger \, dS - \int_{\Omega} \rho (\mathbf{u} \cdot \nabla) \gamma \, d\mathbf{x} = 0, \quad \forall \gamma \in \mathbb{V}_T, \quad (12a)$$

$$\int_{\Omega} \eta \frac{\partial (\rho m)}{\partial t} \, d\mathbf{x} + \int_{\Gamma} (\mathbf{u}^+ \cdot \hat{\mathbf{n}}^+) \llbracket \eta \rrbracket_+ (\rho m)^\dagger \, dS - \int_{\Omega} \rho m (\mathbf{u} \cdot \nabla) \eta \, d\mathbf{x} = 0, \quad \forall \eta \in \mathbb{V}_T. \quad (12b)$$

As \mathbb{V}_T permits discontinuities, the value of a field at a facet may differ depending on which element is considered. As the direction of the flow is not known a priori, the two sides of the facet are arbitrarily labelled as ‘+’ and ‘-’, with $\hat{\mathbf{n}}^+$ denoting an outward normal vector on the + side. Any difference in

a field across the facet is denoted by the jump operator in double square brackets, which for a scalar is $\llbracket \gamma \rrbracket_+ := \gamma^+ - \gamma^-$. The dagger \dagger denotes the upwind value at a facet, e.g.

$$\rho^\dagger := \begin{cases} \rho^+ & \text{if } \mathbf{u}^+ \cdot \hat{\mathbf{n}}^+ \geq 0, \\ \rho^- & \text{if } \mathbf{u}^+ \cdot \hat{\mathbf{n}}^+ < 0. \end{cases} \quad (13)$$

Note, that in general, (12) may include inflow and outflow boundary terms (Gibson et al., 2019), but we do not consider these as we either solve the equations on the sphere, or in a vertical slice with periodic boundary conditions in the horizontal dimension and impermeable, rigid, boundaries in the vertical dimension.

The DG formulations of the conservative transport equation for the dry density (12a) and the conservative tracer transport equation (12b) are shown to be conservative by taking test functions of $\gamma = 1$ and $\eta = 1$. This reduces the transport equations to global conservation statements of

$$\frac{d}{dt} \int_{\Omega} \rho \, d\mathbf{x} = 0, \quad (14a)$$

$$\frac{d}{dt} \int_{\Omega} \rho m \, d\mathbf{x} = 0. \quad (14b)$$

The conservative tracer transport equation (12b) is also consistent, as setting $m = C$ for some spatially constant C and $\eta = 1$ leads to a scaling of the conservative density transport equation (12a).

For completeness, the DG upwind formulation of an advective transport equation for the mixing ratio (3) is

$$\int_{\Omega} \chi \frac{\partial m}{\partial t} \, d\mathbf{x} + \int_{\Gamma} (\mathbf{u}^+ \cdot \hat{\mathbf{n}}^+) \llbracket \chi \rrbracket_+ m^\dagger \, dS - \int_{\Omega} m \nabla \cdot (\chi \mathbf{u}) \, d\mathbf{x} = 0, \quad \forall \chi \in \mathbb{V}_T, \quad (15)$$

with χ a scalar test function. The advective scheme, which solves (12a) and (15), will be compared with the new conservative tracer scheme of (12a) and (12b) in the numerical tests of sections 3 and 4. These tests will show that solving the conservative tracer transport equations in valid function spaces leads to tracer mass conservation and consistency. Obtaining a scheme that also ensures non-negativity requires additional work, and this will be discussed in section 5.

2.4 Time discretisation

For all the tests besides the ‘mock dynamical core’ test in section 6, which solves the compressible Euler equations, we will apply an explicit Runge-Kutta (RK) time discretisation to the DG upwinded transport equations (Cockburn & Shu, 2001). Specifically, we use the third-order strong stability preserving scheme, SSPRK3 (Shu & Osher, 1988). Strong stability preserving RK methods can be expressed as a sequence of forward Euler steps, allowing for higher-order accuracy whilst retaining the strong stability properties of a single forward Euler step (Chapter 2.3.3 of Durran (2010)). Using a multistage time discretisation like an explicit RK method also simplifies the application of limiters to enforce non-negativity (Cotter & Kuzmin, 2016). We denote the one full application of the time discretisation to the transport terms as $\mathcal{T} : \mathbb{V}_T \rightarrow \mathbb{V}_T$.

A key difference between the conservative transport equation for ρ and the conservative tracer transport equation for ρm , is that the latter is nonlinear in the trial function. From an implementation perspective, this requires that the ρ and ρm fields are updated directly as opposed to computing increments, as the change in tracer density cannot be directly used to update the mixing ratio. We denote the isolation of the updated mixing ratio from the updated ρm field by the identification operator of $\mathcal{M} : \mathbb{V}_T \rightarrow \mathbb{V}_T$. Additionally, a different solver is typically required for the conservative tracer transport equation compared to the equations that are linear in the trial function, i.e. the advective transport of m or conservative transport of ρ . We choose the Newton line search algorithm from the PETSc solver library (Balay et al., 1997, 2024) for our nonlinear solver. The solver starts from an initial guess of ρm at the previous timestep or intermediate stage to avoid convergence issues near a zero state.

2.5 Operators for mapping fields between function spaces

We now describe a core component of our conservative tracer transport scheme: the mapping of the dry density and mixing ratios from their original fields into a shared function space for transport, to ensure conservation and consistency. In addition to standard Galerkin projections between function spaces, we introduce three key operations:

- Conservative Galerkin projection: The projection of a mixing ratio between spaces such that the tracer density is conserved.
- Recovery: Mapping a field from a lowest-order to next-to-lowest-order function space.
- Embedded DG: Mapping from a fully or partially continuous space into a fully discontinuous counterpart.

A different composition of these operations will be required for the four different combinations of function spaces for ρ and m (section 2.1). In describing these operations, we define the following types of function space:

- \mathbb{V}_ρ — original space for the dry density ($\mathbb{V}_{\rho,0}/\mathbb{V}_{\rho,1}$)
- \mathbb{V}_m — original space for mixing ratio, either co-located with density ($\mathbb{V}_{\rho,0}/\mathbb{V}_{\rho,1}$) or vertically staggered ($\mathbb{V}_{\theta,0}/\mathbb{V}_{\theta,1}$)
- $\tilde{\mathbb{V}}$ — a higher-order and fully continuous space used in the recovery scheme ($\tilde{\mathbb{V}}_1$)
- $\hat{\mathbb{V}}$ — a fully discontinuous space used in the recovery and embedded DG methods ($\mathbb{V}_{\rho,1}/\hat{\mathbb{V}}_\theta$)
- \mathbb{V}_T — a fully discontinuous space where the transport of ρ and m is performed in ($\mathbb{V}_{\rho,1}/\hat{\mathbb{V}}_\theta$)

The original and transport function spaces used for the four function space combinations of ρ and m are shown in Table 1, whilst Table 2 overviews the operators and their input and output (mapped) function spaces. We now provide further details of the three special operations.

Table 1: Function spaces used for the four combinations of dry density and mixing ratio fields. A recovered space is used to identify a higher-order representation of a $k = 0$ field. An embedded space is used when moving from a fully or partially continuous space into a fully discontinuous space. The space in which the transport is performed is denoted by (T). Fields start and end each timestep in their original space.

Pair of function spaces	Field(s)	Original space	Recovered space	Embedded space
Co-located, order 0	ρ, m	$\mathbb{V}_{\rho,0} = dQ_0 \otimes dQ_0$	$\tilde{\mathbb{V}}_1 := Q_1 \otimes Q_1$	$\mathbb{V}_{\rho,1} := dQ_1 \otimes dQ_1$ (T)
Co-located, order 1	ρ, m	$\mathbb{V}_{\rho,1} := dQ_1 \otimes dQ_1$ (T)	—	—
Vertically staggered, order 0	ρ	$\mathbb{V}_{\rho,0} := dQ_0 \otimes dQ_0$	$\tilde{\mathbb{V}}_1 := Q_1 \otimes Q_1$	$\mathbb{V}_{\rho,1} := dQ_1 \otimes dQ_1$ (T)
	m	$\mathbb{V}_{\theta,0} := dQ_0 \otimes Q_1$	$\tilde{\mathbb{V}}_1 := Q_1 \otimes Q_1$	$\mathbb{V}_{\rho,1} := dQ_1 \otimes dQ_1$ (T)
Vertically staggered, order 1	ρ	$\mathbb{V}_{\rho,1} := dQ_1 \otimes dQ_1$	—	$\hat{\mathbb{V}}_\theta := dQ_1 \otimes dQ_2$ (T)
	m	$\mathbb{V}_{\theta,1} := dQ_1 \otimes Q_2$	—	$\hat{\mathbb{V}}_\theta := dQ_1 \otimes dQ_2$ (T)

Table 2: A list of the key operators used in the advective and conservative tracer transport schemes. The subscript $(\)_{\rho m}$ denotes a conservative version of that operation. Conservative operations for the mixing ratio require the dry density in the original and mapped spaces, so the corresponding operation on the dry density is always performed first, i.e. recovery \mathcal{J}_ρ before conservative recovery $\mathcal{J}_{\rho m}$, injection \mathcal{I}_ρ before conservative injection $\mathcal{I}_{\rho m}$, and projection \mathcal{P}_ρ before conservative projection $\mathcal{P}_{\rho m}$.

Operator	Description
$\mathcal{J} : \mathbb{V} \rightarrow \hat{\mathbb{V}}$	Application of the recovery scheme on a single field
$\mathcal{J}_{\rho m} : \mathbb{V}_m, \mathbb{V}_\rho, \hat{\mathbb{V}} \rightarrow \hat{\mathbb{V}}$	Application of the conservative recovery scheme on m
$\mathcal{I} : \mathbb{V} \rightarrow \hat{\mathbb{V}}$	Injection of a single field into a fully discontinuous space
$\mathcal{I}_{\rho m} : \mathbb{V}_m, \mathbb{V}_\rho, \hat{\mathbb{V}} \rightarrow \hat{\mathbb{V}}$	Conservative injection of m into a fully discontinuous space
$\mathcal{T} : \mathbb{V}_T \rightarrow \mathbb{V}_T$	Transport (advective or conservative tracer)
$\mathcal{M} : \mathbb{V}_T \rightarrow \mathbb{V}_T$	Identification of m from the product ρm
$\mathcal{P} : \mathbb{V}_T \rightarrow \mathbb{V}$	Projection of a single field into its original space
$\mathcal{P}_{\rho m} : \mathbb{V}_T, \mathbb{V}_T, \mathbb{V}_\rho \rightarrow \mathbb{V}_m$	Conservative projection of m into its original space

2.5.1 Conservative Galerkin projection

The primary method for mapping a field between function spaces is with a Galerkin projection. This equates weak form expressions of the field on both the original (\mathbb{V}^O) and mapped (\mathbb{V}^M) function spaces. The Galerkin projection $\mathcal{P} : \mathbb{V}^O \rightarrow \mathbb{V}^M$ of an original field $q^O \in \mathbb{V}^O$ to a mapped field of $q^M \in \mathbb{V}^M$ is

$$\int_{\Omega} \psi q^M \, d\mathbf{x} = \int_{\Omega} \psi q^O \, d\mathbf{x}, \quad \forall \psi \in \mathbb{V}^M. \quad (16)$$

This Galerkin projection ensures that q is conserved globally, and hence is sufficient for projecting the density. However, applying the Galerkin projection to a mixing ratio does not ensure that the tracer mass of $\rho_X = \rho m$ is conserved. Accordingly, we introduce a conservative Galerkin projection of $\mathcal{P}_{\rho m} : \mathbb{V}_m^O, \mathbb{V}_\rho^O, \mathbb{V}_\rho^M \rightarrow \mathbb{V}_m^M$ which requires the density in both the original and mapped spaces. The conservative Galerkin projection is then used to obtain m^M , given m^O, ρ^O, ρ^M fields,

$$\int_{\Omega} \psi m^M \rho^M \, d\mathbf{x} = \int_{\Omega} \psi m^O \rho^O \, d\mathbf{x}, \quad \forall \psi \in \mathbb{V}_m^M. \quad (17)$$

Setting the test function to $\psi = 1$ shows that the conservative Galerkin projection conserves the tracer density. It is important to emphasise that any projection of the dry density (16) must occur before the conservative projection (17), so that we have representations of the density in both the original and mapped spaces. A similar projection to (17) is discussed in Bendall et al. (2023), where ρ_X is mapped between a primary Charney-Phillips grid and a secondary shifted mesh.

Whilst the conservative Galerkin projection achieves mass conservation, it is not necessarily consistent. This is because the projection of a constant higher-order field ($m^O \in \mathbb{V}^H$) is not guaranteed to generate a lower-order field ($m^M \in \mathbb{V}^L$) that is also constant. To resolve this, we note that setting $m^O = 0$ in (17) ensures that m^M must also be zero throughout the domain. If we identify a mean value of the mixing ratio, computed as

$$m_{\bar{\Omega}} = \frac{\int_{\Omega} m^O \, d\mathbf{x}}{\int_{\Omega} 1 \, d\mathbf{x}}, \quad (18)$$

then a spatially constant field will satisfy $m - m_{\bar{\Omega}} = 0$ everywhere in the domain. Thus, consistency

is ensured with a conservative Galerkin projection of

$$\int_{\Omega} \psi \rho^M (m^M - m_{\bar{\Omega}}) d\mathbf{x} = \int_{\Omega} \psi \rho^O (m^O - m_{\bar{\Omega}}) d\mathbf{x}, \quad \forall \psi \in \mathbb{V}^L. \quad (19)$$

The conservative and consistent Galerkin projection (19) is used for the reversible recovery of mixing ratios, which we now discuss.

2.5.2 The recovery scheme

As lowest-order finite element spaces do not allow for the desired second-order (or higher) accuracy for transport equations, we perform all transport in next-to-lowest-order spaces. To accurately map a $k = 0$ field into a $k = 1$ space, we use the recovered space scheme of Bendall et al. (2019). There are two key steps in this scheme. First is the (averaging) recovery operation, $\mathcal{R} : \mathbb{V} \rightarrow \tilde{\mathbb{V}}$, where a $k = 0$ field is represented in a fully continuous $k = 1$ space using the second-order averaging operator of Georgoulis and Pryer (2018). This operation does not conserve the integral of the field, and the discrepancy in the lowest-order space can be computed as $\Delta q_L = q - \tilde{\mathcal{P}}\mathcal{R}q = (1 - \tilde{\mathcal{P}}\mathcal{R})q$, where $\tilde{\mathcal{P}} : \tilde{\mathbb{V}} \rightarrow \mathbb{V}$ projects the averaged $k = 1$ field back into the original $k = 0$ space. An additional consideration of the recovery step is dealing with the boundaries in a manner that retains second-order accuracy, as detailed in Bendall (2019). For recovery in vertical slice domains, a Taylor series expansion is used at the vertical boundaries to ensure sufficient accuracy.

For the discontinuous Galerkin transport, the continuity requirements of the recovered $\tilde{\mathbb{V}}$ function space need to be broken. Hence, the second step of the recovery process is to *inject* the recovered field into a fully discontinuous version of the recovered space, $\mathcal{I} : \tilde{\mathbb{V}} \rightarrow \hat{\mathbb{V}}$. To ensure that the full recovery operation preserves the global integral of the field, the Δq_L mass correction is also injected into the discontinuous transport space. Combining the recovery and injection steps leads to a complete recovered space operator of

$$\mathcal{J} = \mathcal{I}\mathcal{R} + \mathcal{I}(1 - \tilde{\mathcal{P}}\mathcal{R}). \quad (20)$$

Whilst the \mathcal{J} recovery operator is sufficient for recovering lowest-order density fields, a modification is required for mixing ratios to ensure conservation of tracer density. No change is required to the recovery operator \mathcal{R} that obtains the averaged higher-order field, but the injection (\mathcal{I}) and projection ($\tilde{\mathcal{P}}$) operators are replaced with conservative versions of $\mathcal{I}_{\rho m} : \tilde{\mathbb{V}}, \tilde{\mathbb{V}}, \hat{\mathbb{V}} \rightarrow \hat{\mathbb{V}}$ and $\tilde{\mathcal{P}}_{\rho m} : \tilde{\mathbb{V}}, \tilde{\mathbb{V}}, \mathbb{V}_{\rho} \rightarrow \mathbb{V}_m$. The complete conservative recovery operator is

$$\mathcal{J}_{\rho m} = \mathcal{I}_{\rho m}\mathcal{R} + \mathcal{I}_{\rho m}(1 - \tilde{\mathcal{P}}_{\rho m}\mathcal{R}). \quad (21)$$

After applying the transport operator in $\mathbb{V}_T = \hat{\mathbb{V}}$, the updated fields are projected back into their original lowest-order space. This is achieved through a standard Galerkin projection of $\mathcal{P} : \mathbb{V}_T \rightarrow \mathbb{V}_{\rho}$ for the dry density, and a conservative Galerkin projection of $\mathcal{P}_{\rho m} : \mathbb{V}_T, \mathbb{V}_T, \mathbb{V}_{\rho} \rightarrow \mathbb{V}_m$ for conservatively transported mixing ratios. Bendall et al. (2019) gives an alternative projection operator that ensures that no additional maxima or minima are created in this step, but as this operator is not mass-conserving, it will not be used in this work.

2.5.3 The embedded DG scheme

For mixing ratios that lie in a partially continuous \mathbb{V}_{θ} space, we use the *embedded DG* scheme of Cotter and Kuzmin (2016) and its injection operator to map m to the fully discontinuous transport space. This method is only needed for the vertically staggered $k = 1$ case, as the recovery method for $k = 0$ elements already incorporates an injection into a fully discontinuous space for transport (21). For $m \in \mathbb{V}_{\theta,1} := dQ_1 \otimes Q_2$, the injection maps to the $\hat{\mathbb{V}}_{\theta} := dQ_1 \otimes dQ_2$ function space where the vertical continuity constraint is relaxed. We use a conservative injection of $\mathcal{I}_{\rho m} : \mathbb{V}_{\theta,1}, \mathbb{V}_{\rho,1}, \hat{\mathbb{V}}_{\theta} \rightarrow \hat{\mathbb{V}}_{\theta}$ to ensure conservation of tracer density. This requires the density in both the original and transport spaces, so a Galerkin projection on the density of $\mathcal{P} : \mathbb{V}_{\rho,1} \rightarrow \hat{\mathbb{V}}_{\theta}$ is performed before the embedded DG injection. Like with the recovered scheme, the fields are projected back to their original space after the transport is complete, and this requires a conservative projection (17) for the mixing ratio.

3 Conservative transport with co-located spaces

Our first test of the conservative tracer transport scheme considers a dry density and mixing ratio that are co-located in the same fully discontinuous function space. A summary of operations for the advective and conservative tracer schemes is given for $k = 1$ elements in Table 3 and $k = 0$ elements in Table 4. With next-to-lowest-order elements, transport is performed in the original space of $\mathbb{V}_{\rho,1}$, so no other operations are required. For $k = 0$, we employ the recovery scheme.

Table 3: Description of the operations used with co-located $k = 1$ function spaces, starting from original fields of $\rho_1^n, m_1^n \in \mathbb{V}_{\rho,1}$ at time index n . The transport operator acting on a vector in the conservative scheme emphasises that the transport of these fields is coupled. The ‘spaces’ column indicates the input and output function spaces during the step. Dashes in the conservative columns indicate that the operation or spaces are the same as with the advective scheme.

Step	Advective scheme	Spaces	Conservative scheme	Spaces
1. Transport	$\rho_1^{n+1} = \mathcal{T}[\rho_1^n]$ $m_1^{n+1} = \mathcal{T}[m_1^n]$	$\mathbb{V}_{\rho,1} \rightarrow \mathbb{V}_{\rho,1}$	$\begin{bmatrix} \rho_1^{n+1} \\ m_1^{n+1} \end{bmatrix} = \begin{bmatrix} 1 \\ \mathcal{M} \end{bmatrix} \mathcal{T} \begin{bmatrix} \rho_1^n \\ \rho_1^n m_1^n \end{bmatrix}$	—

Table 4: Description of the operations used with co-located $k = 0$ function spaces, starting from original fields of $\rho_0^n, m_0^n \in \mathbb{V}_{\rho,0}$ at time index n . Variables with a $(\)_1$ subscript are recovered from the lowest-order $(\)_0$ space.

Step	Advective scheme	Spaces	Conservative scheme	Spaces
1. Recover ρ	$\rho_1^n = \mathcal{J}[\rho_0^n]$	$\mathbb{V}_{\rho,0} \rightarrow \mathbb{V}_{\rho,1}$	—	—
2. Recover or conservatively recover m	$m_1^n = \mathcal{J}[m_0^n]$	$\mathbb{V}_{\rho,0} \rightarrow \mathbb{V}_{\rho,1}$	$m_1^n = \mathcal{J}_{\rho m}[m_0^n, \rho_0^n, \rho_1^n]$	$\mathbb{V}_{\rho,0}, \mathbb{V}_{\rho,0}, \mathbb{V}_{\rho,1} \rightarrow \mathbb{V}_{\rho,1}$
3. Transport	$\rho_1^{n+1} = \mathcal{T}[\rho_1^n]$ $m_1^{n+1} = \mathcal{T}[m_1^n]$	$\mathbb{V}_{\rho,1} \rightarrow \mathbb{V}_{\rho,1}$	$\begin{bmatrix} \rho_1^{n+1} \\ m_1^{n+1} \end{bmatrix} = \begin{bmatrix} 1 \\ \mathcal{M} \end{bmatrix} \mathcal{T} \begin{bmatrix} \rho_1^n \\ \rho_1^n m_1^n \end{bmatrix}$	—
4. Project ρ	$\rho_0^{n+1} = \mathcal{P}[\rho_1^{n+1}]$	$\mathbb{V}_{\rho,1} \rightarrow \mathbb{V}_{\rho,0}$	—	—
5. Project or conservatively project m	$m_0^{n+1} = \mathcal{P}[m_1^{n+1}]$	$\mathbb{V}_{\rho,1} \rightarrow \mathbb{V}_{\rho,0}$	$m_0^{n+1} = \mathcal{P}_{\rho m}[m_1^{n+1}, \rho_1^{n+1}, \rho_0^{n+1}]$	$\mathbb{V}_{\rho,1}, \mathbb{V}_{\rho,1}, \mathbb{V}_{\rho,0} \rightarrow \mathbb{V}_{\rho,0}$

3.1 Numerical tests

We apply the transport test on the sphere of Nair and Lauritzen (2010) with co-located spaces. This test considers only transport terms to directly compare the conservative and advective form schemes for the tracer transport. We run two versions of the test: first, the convergence setting, which tests mass conservation and the order of the scheme convergence, and second, the consistency setting, to check the preservation of a constant mixing ratio.

An equiangular gnomonic cubed-sphere mesh (Ronchi et al., 1996) is used, with quadrilateral Raviart-Thomas elements to represent the velocity field. The velocity is prescribed using a modified

divergent flow field from Nair and Lauritzen (2010), leaving the density and mixing ratio as the only prognostic variables. The flow field is defined such that a scalar field will be transported back to its original location at the end time. Hence, any deviation from the initial condition can be used to measure the transport error. In the convergence setting, two Gaussian perturbations are applied to the mixing ratio field, whilst the consistency test uses a constant mixing ratio field with a perturbed density. Further details on the test case setup are found in Appendix A.1.

Figure 2 shows the L2 error in the final mixing ratio fields, which are virtually identical for both the advective and conservative tracer schemes. Second-order convergence is obtained with $k = 0$ elements, verifying that the recovery scheme of Bendall et al. (2019) allows for higher-order transport accuracy with the lowest-order fields. The convergence rate for the $k = 1$ spaces, where transport takes place in the original space for both ρ and m , is better than second-order. Figure 2 also plots the mean tracer density error over the simulation (9). The conservative tracer transport scheme preserves the tracer density to near machine precision with both element orders, showing that there is very good mass conservation. Contrastingly, there are significantly larger mass discrepancies with the advective scheme. For the consistency test, Figure 3 shows that both the advective and conservative tracer methods preserve the constant mixing ratio to a high level of accuracy. The consistency error is larger for the conservative method when $k = 0$, due to the mappings in the recovery scheme, but remains sufficiently small.

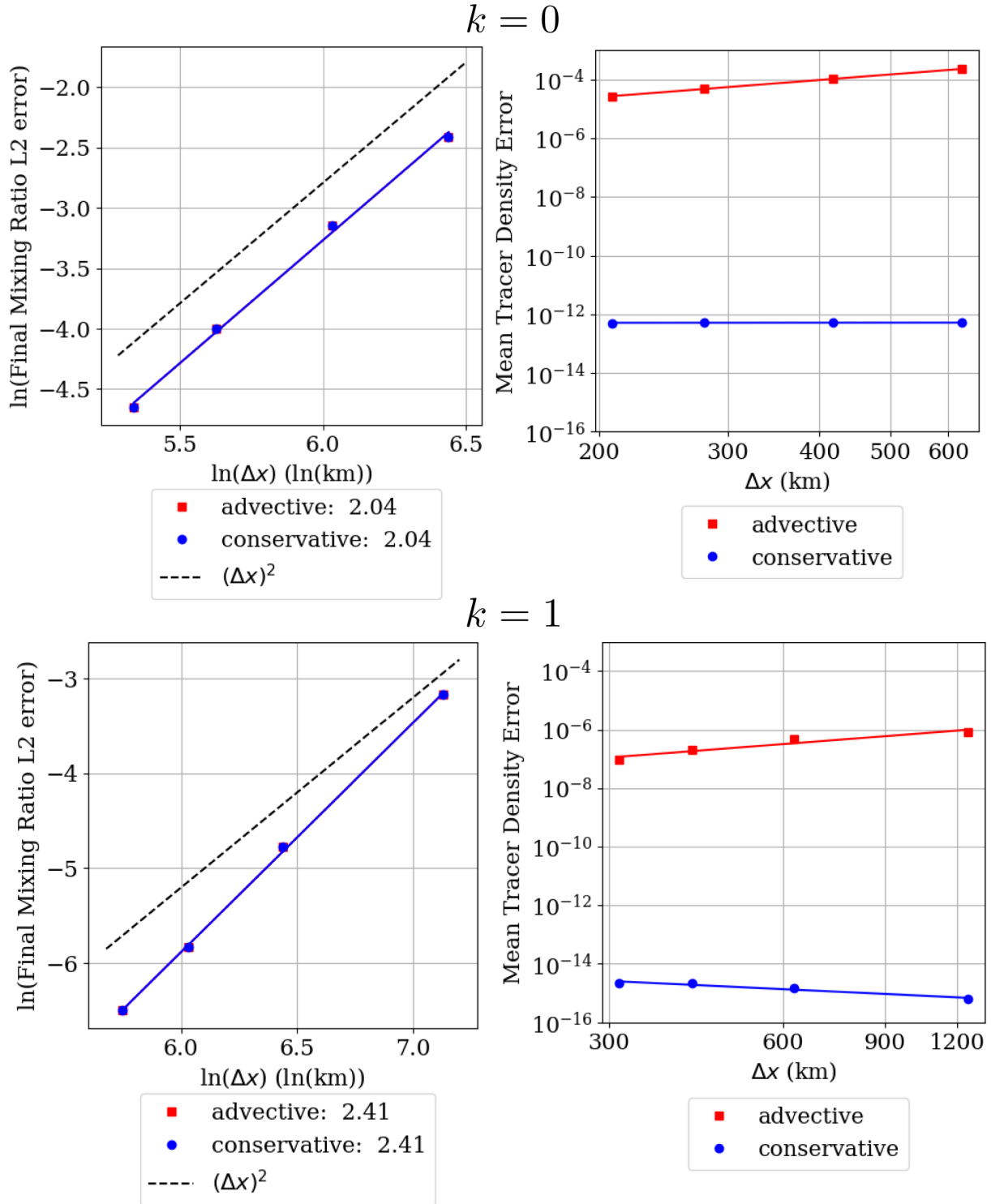


Figure 2: L2 mixing ratio error (left column) and mean tracer density error (right column) in the co-located transport-only tests. Lowest-order elements are shown in the top row and next-to-lowest-order in the bottom row. A characteristic cell length for the cubed-sphere is computed as $\Delta x = \pi R/2N_e$, where N_e is the number of cells per panel edge. Legend values in the L2 error plots denote the approximate order of convergence from a line of best fit. For both element orders, the conservative tracer scheme shows good mass conservation, as shown by small errors in the tracer density. Larger tracer density errors are present when using $k = 0$ spaces, which requires the recovery scheme, compared to $k = 1$ spaces, where the fields are transported in their original spaces.

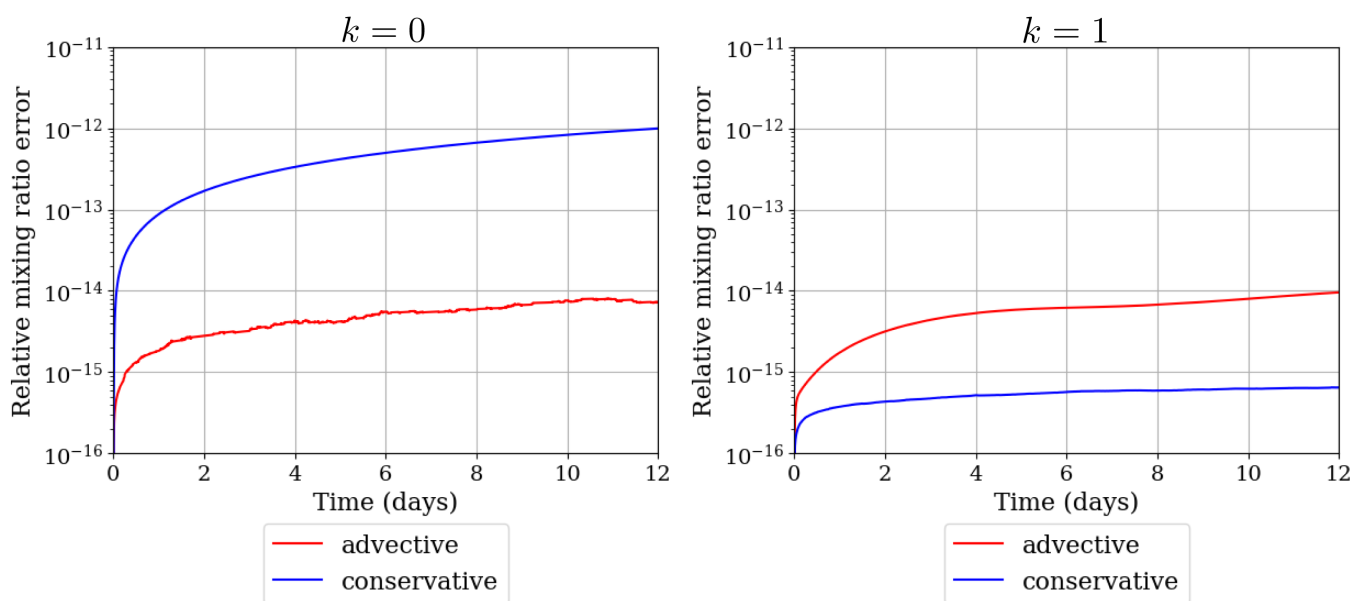


Figure 3: Co-located transport-only test with the consistency configuration, in which the mixing ratio is held constant while the density is spatially varying. Lowest-order elements are shown on the left and next-to-lowest-order on the right. Both the advective and conservative tracer schemes preserve a constant mixing ratio to a high level of accuracy.

4 Conservative transport with vertically staggered spaces

We now move to the case where the density and mixing ratio lie in different function spaces, with the mixing ratio in the thermodynamic space of a Charney-Phillips vertical staggering. A summary of operations for the advective and conservative tracer schemes is given for $k = 1$ in Table 5 and $k = 0$ in Table 6.

For next-to-lowest-order elements, simply transporting the fields in their original spaces — $m \in \mathbb{V}_{\theta,1}$ and $\rho \in \mathbb{V}_{\rho,1}$ — actually leads to very good mass conservation in this test. However, this choice performs poorly in the consistency test. Hence, to ensure both mass conservation and consistency, we require the transport of ρ and m in the same function space. The conservative embedded DG scheme is used here, which injects m from the partially continuous $\mathbb{V}_{\theta,1}$ space to the fully discontinuous $\hat{\mathbb{V}}_{\theta}$ space. The density is also projected to the transport space, using $\mathcal{P} : \mathbb{V}_{\rho,1} \rightarrow \hat{\mathbb{V}}_{\theta}$. The recovery scheme is again used with the lowest-order elements.

Table 5: Description of the operations used with vertically staggered $k = 1$ function spaces, starting from original fields $\rho_1^n \in \mathbb{V}_{\rho,1}$, $m_1^n \in \mathbb{V}_{\theta,1}$ at time index n . The $(\)_1$ subscripts denote fields in their original space, with $(\hat{\ })$ denoting fields in the fully discontinuous transport space.

Step	Advective scheme	Spaces	Conservative scheme	Spaces
1. Project ρ	$\hat{\rho}^n = \mathcal{P}[\rho_1^n]$	$\mathbb{V}_{\rho,1} \rightarrow \hat{\mathbb{V}}_{\theta}$	—	—
2. Inject or conservatively inject m	$\hat{m}^n = \mathcal{I}[m_1^n]$	$\mathbb{V}_{\theta,1} \rightarrow \hat{\mathbb{V}}_{\theta}$	$\hat{m}^n = \mathcal{I}_{\rho m}[m_1^n, \rho_1^n, \hat{\rho}^n]$	$\mathbb{V}_{\theta,1}, \mathbb{V}_{\rho,1}, \hat{\mathbb{V}}_{\theta} \rightarrow \hat{\mathbb{V}}_{\theta}$
3. Transport	$\hat{\rho}^{n+1} = \mathcal{T}[\hat{\rho}^n]$ $\hat{m}^{n+1} = \mathcal{T}[\hat{m}^n]$	$\hat{\mathbb{V}}_{\theta} \rightarrow \hat{\mathbb{V}}_{\theta}$	$\begin{bmatrix} \hat{\rho}^{n+1} \\ \hat{m}^{n+1} \end{bmatrix} = \begin{bmatrix} 1 \\ \mathcal{M} \end{bmatrix} \mathcal{T} \begin{bmatrix} \hat{\rho}^n \\ \hat{\rho}^n \hat{m}^n \end{bmatrix}$	—
4. Project ρ	$\rho_1^{n+1} = \mathcal{P}[\hat{\rho}^{n+1}]$	$\hat{\mathbb{V}}_{\theta} \rightarrow \mathbb{V}_{\rho,1}$	—	—
5. Project or conservatively project m	$m_1^{n+1} = \mathcal{P}[\hat{m}^{n+1}]$	$\hat{\mathbb{V}}_{\theta} \rightarrow \mathbb{V}_{\theta,1}$	$m_1^{n+1} = \mathcal{P}_{\rho m}[\hat{m}^{n+1}, \hat{\rho}^{n+1}, \rho_1^{n+1}]$	$\hat{\mathbb{V}}_{\theta}, \hat{\mathbb{V}}_{\theta}, \mathbb{V}_{\rho,1} \rightarrow \mathbb{V}_{\theta,1}$

4.1 Numerical tests

Our test with vertically staggered spaces uses a vertical slice modification of the co-located test of section 3.1, as proposed in Bendall et al. (2023). The vertical slice uses a horizontal-vertical (x,z) Cartesian coordinate system and allows the mixing ratio to be defined in the $\mathbb{V}_{0,\theta}$ and $\mathbb{V}_{1,\theta}$ spaces that are discontinuous in x and continuous in z . We again run the test in two configurations — the convergence and consistency settings — to test the mass conservation and consistency properties, respectively. Further details of the test case setup can be found in Appendix A.2.

Figure 4 shows the L2 error in the final mixing ratio field and the mean tracer density error for the $k = 1$ and $k = 0$ cases, respectively. Both transport schemes have the same convergence rates, which are slightly higher than in the co-located tests (Figure 2). The conservative tracer scheme has mass conservation that is close to machine precision for both element orders, showing that the new scheme is mass-conserving with a vertical staggering of ρ and m . For the consistency test, Figure 5 shows that with both element orders, the conservative transport scheme preserves the constant mixing ratio field much better than the advective scheme. The advective scheme is much less consistent than it was with co-located function spaces (Figure 3).

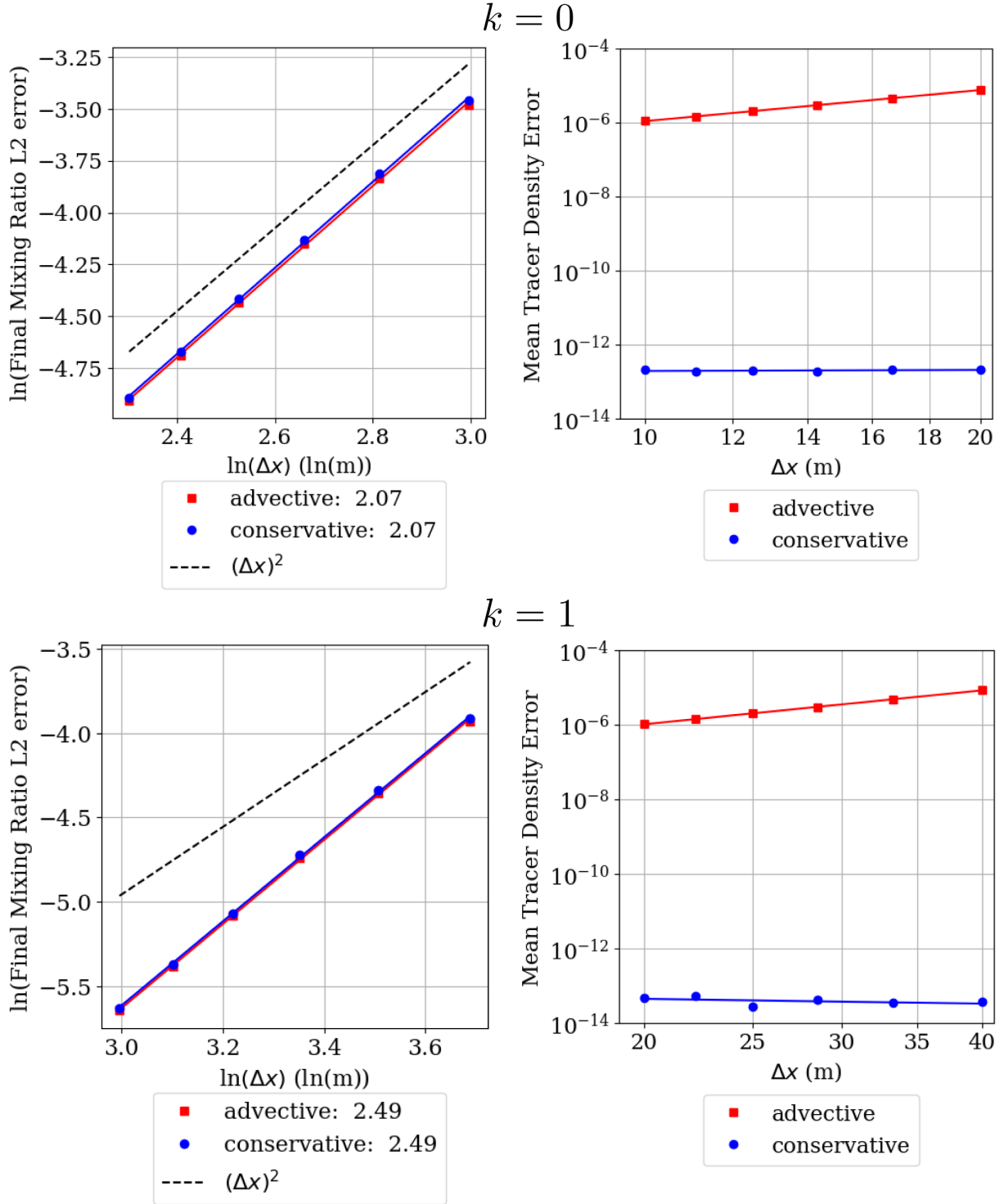


Figure 4: L2 mixing ratio error (left column) and mean tracer density error (right column) in the vertically staggered transport-only tests. Lowest-order elements are shown in the top row and next-to-lowest-order in the bottom row. Legend values in the L2 error plots denote the approximate order of convergence from a line of best fit. For both element orders, the conservative tracer scheme shows good mass conservation, as shown by very small errors in the tracer density.

Table 6: Description of the operations used with vertically staggered $k = 0$ function spaces, starting from original fields $\rho_0^n \in \mathbb{V}_{\rho,0}$, $m_0^n \in \mathbb{V}_{\theta,0}$ at time index n . The subscript $(\)_0$ denotes fields in their original lowest-order space, and the subscript $(\)_1$ denotes the next-to-lowest-order space.

Step	Advective scheme	Spaces	Conservative scheme	Spaces
1. Recover ρ	$\rho_1^n = \mathcal{J}[\rho_0^n]$	$\mathbb{V}_{\rho,0} \rightarrow \mathbb{V}_{\rho,1}$	—	—
2. Recover or conservatively recover m	$m_1^n = \mathcal{J}[m_0^n]$	$\mathbb{V}_{\theta,0} \rightarrow \mathbb{V}_{\rho,1}$	$m_1^n = \mathcal{J}_{\rho m}[m_0^n, \rho_0^n, \rho_1^n]$	$\mathbb{V}_{\theta,0}, \mathbb{V}_{\rho,0}, \mathbb{V}_{\rho,1}$ $\rightarrow \mathbb{V}_{\rho,1}$
3. Transport	$\rho_1^{n+1} = \mathcal{T}[\rho_1^n]$ $m_1^{n+1} = \mathcal{T}[m_1^n]$	$\mathbb{V}_{\rho,1} \rightarrow \mathbb{V}_{\rho,1}$	$\begin{bmatrix} \rho_1^{n+1} \\ m_1^{n+1} \end{bmatrix} = \begin{bmatrix} 1 \\ \mathcal{M} \end{bmatrix} \mathcal{T} \begin{bmatrix} \rho_1^n \\ \rho_1^n m_1^n \end{bmatrix}$	—
4. Project ρ	$\rho_0^{n+1} = \mathcal{P}[\rho_1^{n+1}]$	$\mathbb{V}_{\rho,1} \rightarrow \mathbb{V}_{\rho,0}$	—	—
5. Project or conservatively project m	$m_0^{n+1} = \mathcal{P}[m_1^{n+1}]$	$\mathbb{V}_{\rho,1} \rightarrow \mathbb{V}_{\theta,0}$	$m_0^{n+1} = \mathcal{P}_{\rho m}[m_1^{n+1}, \rho_1^{n+1}, \rho_0^{n+1}]$	$\mathbb{V}_{\rho,1}, \mathbb{V}_{\rho,1}, \mathbb{V}_{\rho,0}$ $\rightarrow \mathbb{V}_{\theta,0}$

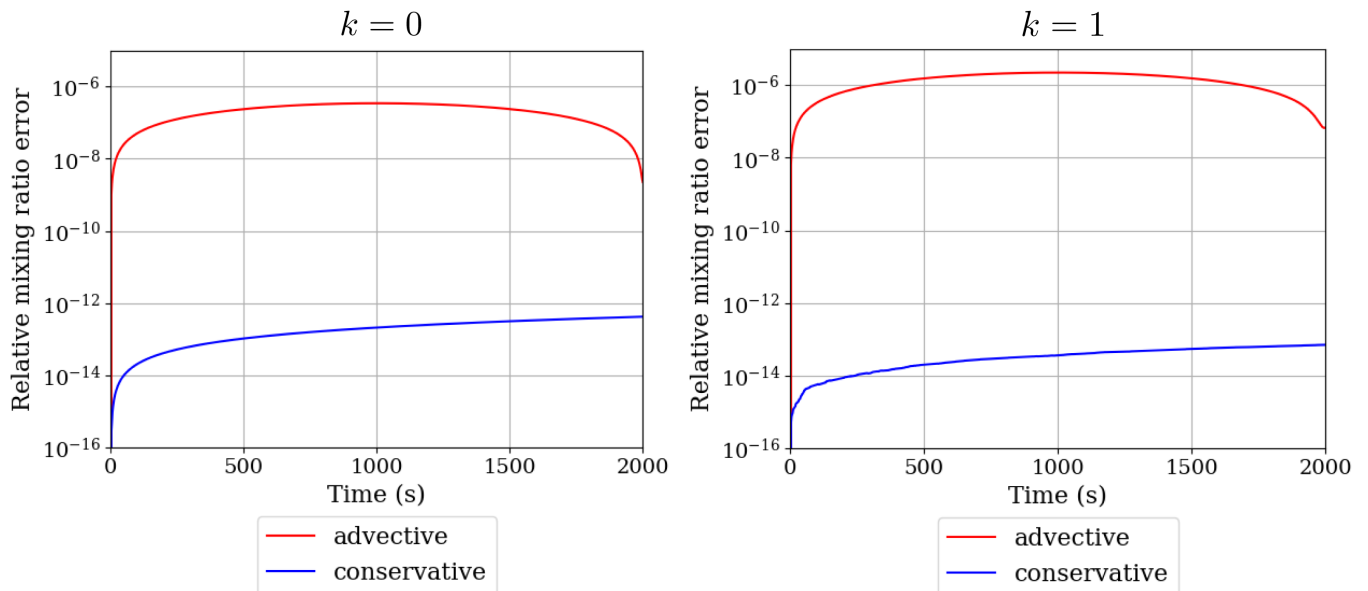


Figure 5: Vertically staggered transport-only test with the consistency configuration, in which the mixing ratio is held constant while the density is spatially varying. Lowest-order elements are shown on the left and next-to-lowest-order on the right. The conservative tracer scheme preserves the constant mixing ratio to a good level of accuracy for both element orders.

5 Non-negativity and physics terms

Now that the convergence and consistency properties of the conservative tracer transport scheme have been tested, we move to the third desirable property: non-negativity. In a general flow, the transport step often generates spurious negative values. The challenge is to remove any negativity in the mixing ratio whilst maintaining conservation and consistency. We address this in the conservative tracer transport scheme through a mean mixing ratio limiter.

We also consider the addition of forcing terms to the transport equation, which are called physics terms in a dynamical core. The presence of physics terms makes the equations more challenging to solve and provides another potential source for negativity in the field.

5.1 A mean mixing ratio limiter

Non-negativity of a field after DG transport can be enforced through a range of limiters; see Cotter and Kuzmin (2016) and references therein for examples. However, even if such methods ensure that the global integral of the field is conserved, they do not ensure conservation of the tracer density of ρm . Hence, we require a method for limiting that ensures conservation of tracer mass as well as non-negativity. A similar challenge to the conservative limiting of tracers was encountered in Brown et al. (2024) and Herrington et al. (2019) when coupling physics and dynamics between meshes of different resolution.

Our approach for conservative limiting is similar to that of Brown et al. (2024), where a fine resolution, and possibly negative, field was combined with a coarser field that was guaranteed to be non-negative. Instead of different resolutions, our approach combines fields from different order function spaces. As a $k = 1$ field may become negative after a transport step, we then blend it with a non-negative $k = 0$ field such that the final next-to-lowest-order field is non-negative. It may be tempting to define the $k = 0$ field at the beginning of the timestep and transport this, as transport in lowest-order spaces is guaranteed to not generate negative values. However, even though $\int_{\Omega} \rho_X \, d\mathbf{x}$ will be the same in both the lower and higher order fields after transport, the tracer density *per cell* will vary, as transport with lowest-order elements is more diffusive. Hence, we compute the $k = 0$ field, which we term the mean mixing ratio (MMR), after transport.

Consider the computation of an MMR of $\bar{m} \in \mathbb{V}_{\rho,0}$ from a $k = 1$ field of $m \in \mathbb{V}_{\rho,1}$, using a conservative, consistent, Galerkin projection (19),

$$\int_{\Omega} \psi \rho (\bar{m} - m_{\bar{\Omega}}) \, d\mathbf{x} = \int_{\Omega} \psi \rho (m - m_{\bar{\Omega}}) \, d\mathbf{x}, \quad \forall \psi \in \mathbb{V}_{\rho,0}, \quad (22)$$

where the same density field of $\rho \in \mathbb{V}_{\rho,1}$ is used on both sides of the equation, and $m_{\bar{\Omega}}$ is the *global* mean (18) that enforces consistency. This definition of the mean mixing ratio (22) ensures that $\bar{\rho}_X = \rho \bar{m}$ represents the same mass per cell as $\rho_X = \rho m$. It is guaranteed that \bar{m} will be non-negative as long as the total mass per cell is non-negative.

We now discuss the blending operation of $\Lambda : \mathbb{V}_{\rho,1}, \mathbb{V}_{\rho,0} \rightarrow \mathbb{V}_{\rho,1}$, which identifies a non-negative mixing ratio field from a linear combination of m and \bar{m} . Consider a blending function in the lowest-order space, $\lambda_m \in \mathbb{V}_{\rho,0}$, which takes a value in $[0, 1]$ in each cell. We apply the blending operation of Brown et al. (2024), where a non-negative mixing ratio of m^* is constructed as

$$m^* = (1 - \lambda_m)m + \lambda_m \bar{m}. \quad (23)$$

The next-to-lowest-order field is unchanged when $\lambda_m = 0$, meaning that higher-order accuracy is retained when the transported field remains non-negative.

To construct the blending function, the minimum value in each cell is computed as the minimum value of m evaluated at the set of cell vertices, I_V . The cell vertices are used instead of the standard $\mathbb{V}_{\rho,1}$ nodes, which do not capture the cell extrema. To obtain non-negativity, we enforce that if $\min_{i \in I_V} \{m_i\} < 0$, then $\min_{i \in I_V} \{m_i^*\} = 0$. From the definition of the blended field (23), this constrains

λ_m in each cell to be

$$\lambda_m = \begin{cases} \frac{-m}{\bar{m} - m}, & \text{if } \min_{i \in IV} \{m_i\} < 0, \\ 0, & \text{else.} \end{cases} \quad (24)$$

New mean mixing ratio fields are computed after each application of the transport operator. For explicit RK schemes, this means computing \bar{m} (22) and applying the MMR limiter (23) after each intermediate step.

5.2 MMR transport test

We now test the MMR limiter in a similar setup to the convergence $k = 1$ configuration of the co-located transport-only test of section 3, but now with a slotted cylinder initial condition, given in Appendix A.3. Discontinuities in the initial mixing ratio field, which is zero in most of the domain, mean that negatives are easily generated during transport. The conservative tracer transport scheme is used for the mixing ratio, and simulations with no limiting and with the MMR limiter are compared. The use of the MMR limiter ensures non-negativity in the mixing ratio field (Figure 6), whilst accurately preserving the integrated tracer density (Figure 7).

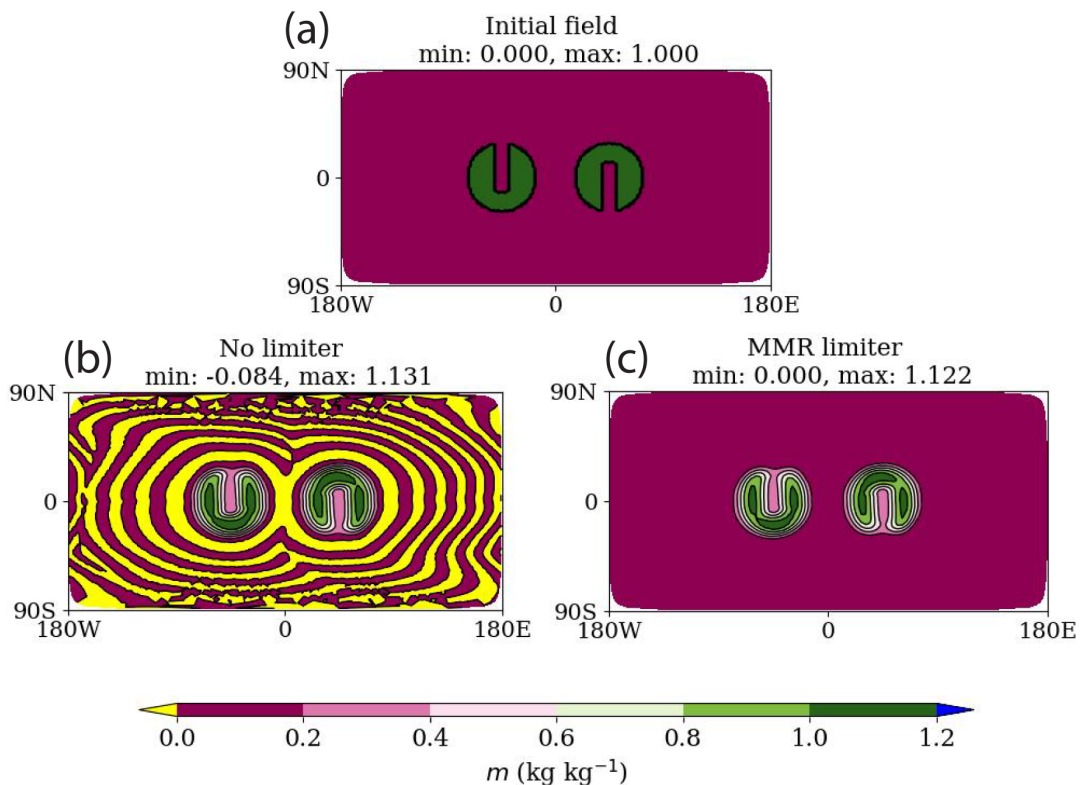


Figure 6: The initial mixing ratio field (a) from the MMR transport test, along with the final mixing ratio fields with no limiter (b) and the MMR limiter (c). The final mixing ratio fields are similar with and without the MMR limiter. The key difference is that the simulation without a limiter allows $m < 0$ (shown in yellow) whilst the MMR limiter has enforced non-negativity.

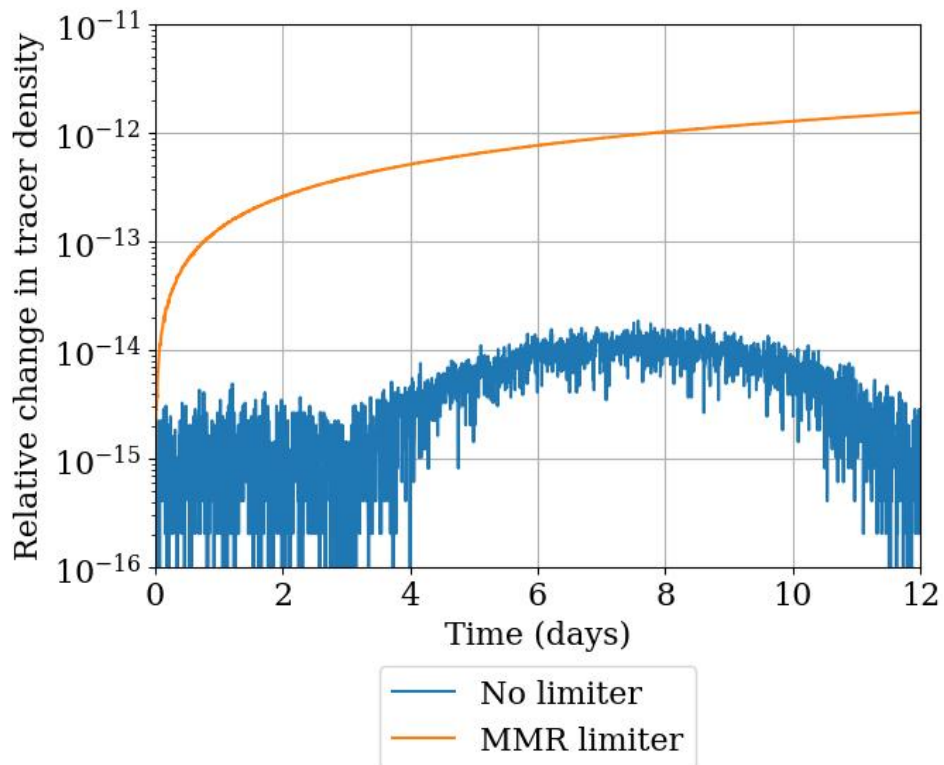


Figure 7: Examining the change in tracer density during the MMR transport test. The case with no limiter has machine precision conservation of tracer density, reflecting the use of the conservative tracer transport equation. The use of the MMR limiter, which ensures non-negativity in the mixing ratio, also preserves the tracer density to a good level of accuracy.

5.3 Terminator Toy chemistry test

We now test the mean mixing ratio limiter in the terminator toy chemistry test of Lauritzen et al. (2015). This test transports two molecular species, specified through mixing ratios of X and X_2 , on a spherical domain. X is a single atom species and X_2 is comprised of two atoms, so the total mixing ratio is $X_T = X + 2X_2$. The exchange of molecules between species X and X_2 is governed by a pair of ODEs that preserve the tracer density of $\rho_X = \rho X_T$.

We use next-to-lowest-order elements and co-located variables of $\rho, X, X_2 \in \mathbb{V}_{\rho,1}$. For the transport step, the advective scheme solves

$$\frac{\partial \rho}{\partial t} + \nabla \cdot (\rho \mathbf{u}) = 0, \quad (25a)$$

$$\frac{\partial X}{\partial t} + (\mathbf{u} \cdot \nabla) X = 0, \quad (25b)$$

$$\frac{\partial X_2}{\partial t} + (\mathbf{u} \cdot \nabla) X_2 = 0, \quad (25c)$$

whilst the conservative tracer scheme solves

$$\frac{\partial \rho}{\partial t} + \nabla \cdot (\rho \mathbf{u}) = 0, \quad (26a)$$

$$\frac{\partial (\rho X)}{\partial t} + \nabla \cdot (\rho X \mathbf{u}) = 0, \quad (26b)$$

$$\frac{\partial (\rho X_2)}{\partial t} + \nabla \cdot (\rho X_2 \mathbf{u}) = 0. \quad (26c)$$

The physics terms in this system are the coupled chemical ODEs governing the molecular interactions,

$$\frac{dX}{dt} = 2f_X, \quad (27a)$$

$$\frac{dX_2}{dt} = -f_X, \quad (27b)$$

where $f_X = k_1 X_2 - k_2 X^2$, and k_1, k_2 are reaction rates given in Appendix A.4. The chemistry ODEs are mass-conserving, as combining (27a) with twice (27b) shows that $dX_T/dt = 0$. The spatial profile of k_1 contains strong gradients, making this a challenging test for transport schemes as numerical error can easily generate spurious negative values.

As the chemical ODEs (27) are too stiff to solve explicitly with a reasonable timestep size, f_X is computed from implicit forcing expressions given in Appendix D of Lauritzen et al. (2015). To ensure that the physics step does not introduce negative values in the mixing ratio fields, f_X is bounded using

$$f_X = \begin{cases} \max \left\{ f_X, -\frac{X}{\Delta t} \right\}, & \text{if } f_X < 0, \\ \min \left\{ f_X, \frac{2X_2}{\Delta t} \right\}, & \text{else.} \end{cases} \quad (28)$$

A cubed-sphere mesh is used with 24 cells per panel edge and a timestep of 450 s. Further details about the test case setup are found in Appendix A.4. We again use the SSPRK3 timestepping scheme for the transport equations. After each full transport step, the physics terms (27) are computed and used to update the X and X_2 fields in a forward Euler step. For the advective scheme, the positive-definite slope limiter of Kuzmin (2010) is applied to all three fields. The advective scheme limiter is more diffusive than the MMR limiter in this test, which is reflected in smaller maximum

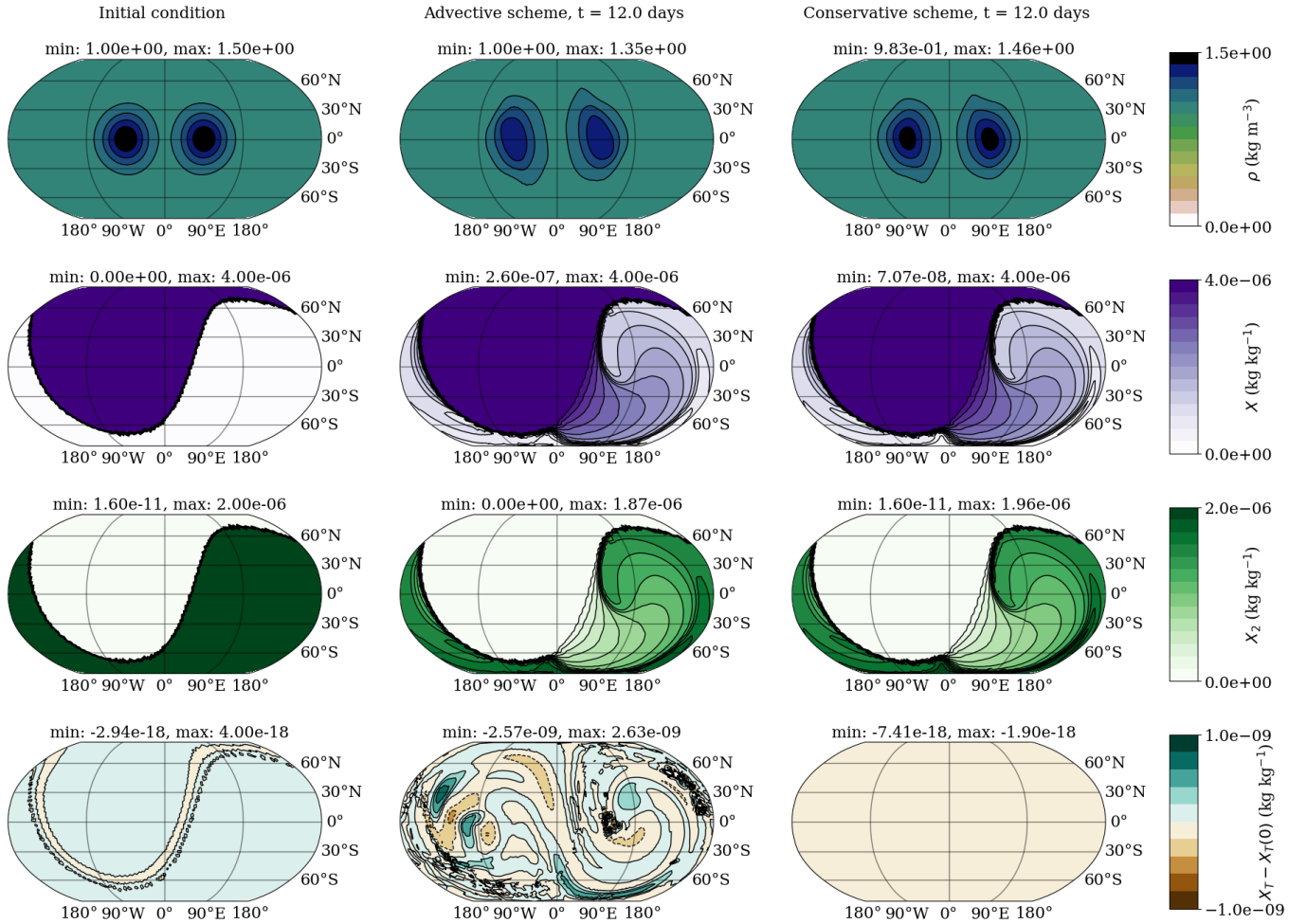


Figure 8: Plots of the density and mixing ratios for the tracer species (X , X_2) in the terminator toy test, visualised with a Robinson projection of the sphere. The left-hand column shows the initial condition, the middle column the final state with the advective scheme, and the right-hand column the final state with the conservative tracer scheme. The first row shows the density fields, with differences between the schemes arising from diffusion introduced by the limiter. The middle two rows plot X and X_2 , showing that both schemes avoid negative mixing ratios. The last row plots the change in total tracer density, $X_T - X_T(0)$. Whilst the advective scheme leads to significant changes in the total tracer density, the difference with the conservative transport scheme remains negligibly small.

values of ρ and X_2 , and a larger minimum value of X in the final states (Figure 8). Otherwise, the final solutions with the advective and conservative tracer schemes are similar, and both ensure non-negative mixing ratios. Figure 9 plots the time series of the total tracer density, $\int_{\Omega} \rho(X + 2X_2) d\mathbf{x}$, with the conservative scheme showing good mass conservation in this test. Interestingly, the conservation of both methods is similar up to the end of day two, at which time the advective scheme rapidly deviates from a conserved ρ_X .

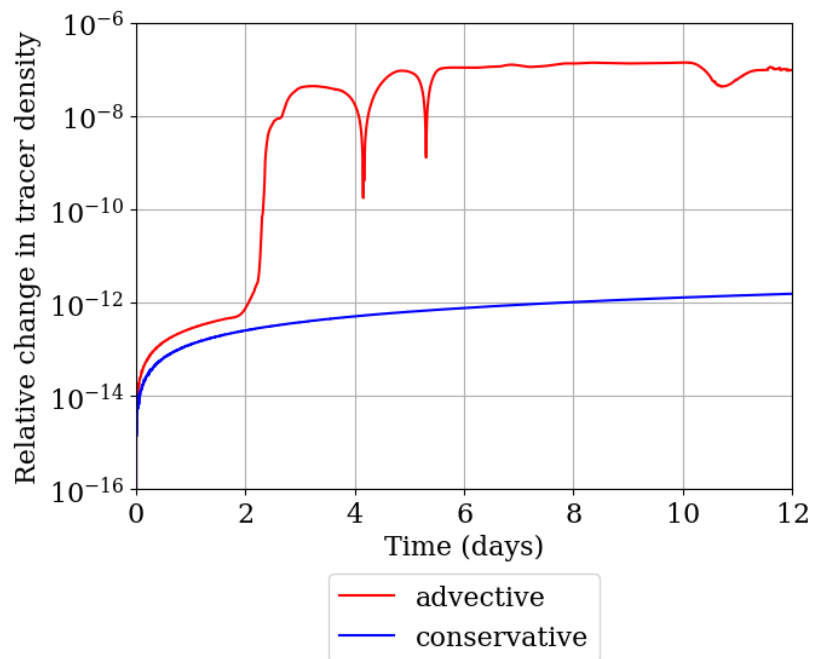


Figure 9: Time series of the relative change in the tracer density for the advective and conservative tracer transport schemes in the terminator toy test. The conservative tracer scheme preserves the total molecular mass of $\int_{\Omega} \rho(X + 2X_2) \, d\mathbf{x}$ to a good level of accuracy.

6 Dynamical core test

As a final test, we apply the conservative tracer transport scheme in a nonhydrostatic dynamical core setup. This solves the compressible Euler equations in a vertical slice domain, without the Coriolis force, and coupled to a single physics scheme of saturation adjustment. We follow the governing equations outlined in Bendall et al. (2020), but neglect the rain moisture species.

The prognostic variable set is $[\mathbf{u}, \rho, \theta_{\text{vd}}, m_{\text{v}}, m_{\text{c}}]$, with $\mathbf{u} = [u, w]^T$ the velocity in the vertical slice, ρ the dry air density, θ_{vd} the virtual dry potential temperature, and m_{v} and m_{c} are mixing ratios for the moisture species of water vapour and cloud water, respectively. To conserve water mass, we require that the global integral of the tracer density, $\rho_X = \rho(m_{\text{v}} + m_{\text{c}})$, is constant in time. We use a vertical staggering of the mixing ratios from the dry density, so $\theta_{\text{vd}}, m_{\text{v}}, m_{\text{c}} \in \mathbb{V}_\theta$ and $\rho \in \mathbb{V}_\rho$. Unlike the previous transport tests where the velocity was prescribed, the velocity is now a prognostic field defined on the Raviart-Thomas function space.

The governing equations, using the advective form for the transport of mixing ratios, are

$$\frac{\partial \mathbf{u}}{\partial t} + (\mathbf{u} \cdot \nabla) \mathbf{u} + \frac{c_p \theta_{\text{vd}}}{1 + m_{\text{v}} + m_{\text{c}}} \nabla \Pi + g \hat{\mathbf{k}} = \mathbf{0}, \quad (29a)$$

$$\frac{\partial \rho}{\partial t} + \nabla \cdot (\mathbf{u} \rho) = 0, \quad (29b)$$

$$\frac{\partial \theta_{\text{vd}}}{\partial t} + (\mathbf{u} \cdot \nabla) \theta_{\text{vd}} + \mu \theta_{\text{vd}} (\nabla \cdot \mathbf{u}) = S_\theta, \quad (29c)$$

$$\frac{\partial m_{\text{v}}}{\partial t} + (\mathbf{u} \cdot \nabla) m_{\text{v}} = S_{\text{v}}, \quad (29d)$$

$$\frac{\partial m_{\text{c}}}{\partial t} + (\mathbf{u} \cdot \nabla) m_{\text{c}} = S_{\text{c}}, \quad (29e)$$

with c_p the specific heat capacity of dry air, $\hat{\mathbf{k}}$ the unit vector in the vertical z -coordinate, and Π the Exner pressure. The quantity of μ in the thermodynamic equation is

$$\mu = \frac{R_{\text{m}}}{c_{\text{vml}}} - \frac{R_{\text{d}} c_{\text{pml}}}{c_{\text{p}} c_{\text{vml}}}, \quad (30)$$

with R_{m} a specific gas constant, R_{d} the ideal gas constant for dry air, and $c_{\text{vml}}, c_{\text{pml}}$ representing specific heat capacities for moist air, at constant pressure and constant volume, respectively.

The S terms in (29) comprise the saturation adjustment physics scheme, which computes the condensation of water vapour to cloud water (S_{c}), the evaporation of cloud water to water vapour (S_{v}), and the effect of latent heat change on the virtual dry potential temperature (S_θ). The physics scheme ensures that mass is not lost during the water phase changes, so $S_{\text{v}} + S_{\text{c}} = 0$. General details of the saturation adjustment scheme can be found in Bryan and Fritsch (2002), with the finite element formulation we use given in Bendall et al. (2020).

To close the compressible Euler equation set, we have an equation of state for the Exner pressure,

$$\Pi = \left(\frac{\rho R_{\text{d}} \theta_{\text{vd}}}{p_0} \right)^{\frac{\kappa}{1-\kappa}}, \quad (31)$$

where $p_0 = 1000$ hPa is a reference pressure, and $\kappa = R_{\text{d}}/c_p$. The Exner pressure is computed diagnostically from the ρ and θ_{vd} fields, which are vertically staggered on the Charney-Phillips grid. We choose $\Pi \in \mathbb{V}_\rho$ to co-locate the Exner pressure with the density, so the projection $\mathcal{P} : \mathbb{V}_\theta \rightarrow \mathbb{V}_\rho$ is applied to θ_{vd} before evaluating Π (31).

As the compressible Euler equations support fast acoustic waves, explicit timesteppers like SSPRK3 are restricted to much smaller timesteps for stability than in the previous tests. As such, we use a semi-implicit quasi-Newton (SIQN) timestepper (Hartney et al., 2025; Melvin et al., 2019; Wood et al., 2014), which mirrors the timestepping methodology of GungHo. The SIQN timestepper consists of an outer loop for the slower transport terms, and an inner loop where the fast dynamics is

solved implicitly. For the compressible Euler equations, the pressure gradient ($\nabla\Pi$) and gravity ($g\hat{\mathbf{k}}$) terms from the momentum equation (29a) are solved in the inner loop. The outer loop solves a transport equation for each prognostic variable, with the moisture species transport for the conservative transport scheme using

$$\frac{\partial(\rho m_v)}{\partial t} + \nabla \cdot (\rho m_v \mathbf{u}) = 0, \quad (32a)$$

$$\frac{\partial(\rho m_c)}{\partial t} + \nabla \cdot (\rho m_c \mathbf{u}) = 0. \quad (32b)$$

The SIQN method is typically used with two inner and two outer loops in GungHo and Gusto. However, as the linear solver used for the inner loop is not mass-conserving, we instead use sixteen outer loops and one inner loop to ensure that the linear solver has minimal impact on the conservation of water mass. Physics increments from the saturation adjustment scheme are applied explicitly, using a forward Euler discretisation, after each full SIQN step. Limiters are not required in this test. Further details of the test case setup and SIQN timestepping are given in Appendix A.5.

This test uses an equivalent sequence of operations to the vertically staggered transport-only cases (Tables 5 and 6), so injections and conservative injections are used for $k = 1$ and recovery and conservative recovery for $k = 0$. The space used to transport ρ , m_v , and m_c for $k = 1$ is $\mathbb{V}_T = \hat{\mathbb{V}}_\theta$, whilst $\mathbb{V}_T = \mathbb{V}_{\rho,1}$ is used in the $k = 0$ test. We also transport θ_{vd} in \mathbb{V}_T , although this is not necessary for tracer mass conservation. For $k = 0$, the velocity field is recovered into a vector equivalent of the $\mathbb{V}_{\rho,1}$ space.

To compare the use of advective and conservative tracer transport, plots of the wet equivalent potential temperature θ_e (Bryan & Fritsch, 2002; Durran & Klemp, 1982) are shown at the end of $k = 0$ and $k = 1$ simulations in Figure 10. In both instances, the final θ_e fields from the advective and conservative tracer transport schemes are very similar. However, Figure 11 shows there is a marked difference in mass conservation; the conservative tracer scheme leads to negligible error in the integrated tracer density for both element orders, whilst the advective scheme leads to a significant change in water mass.

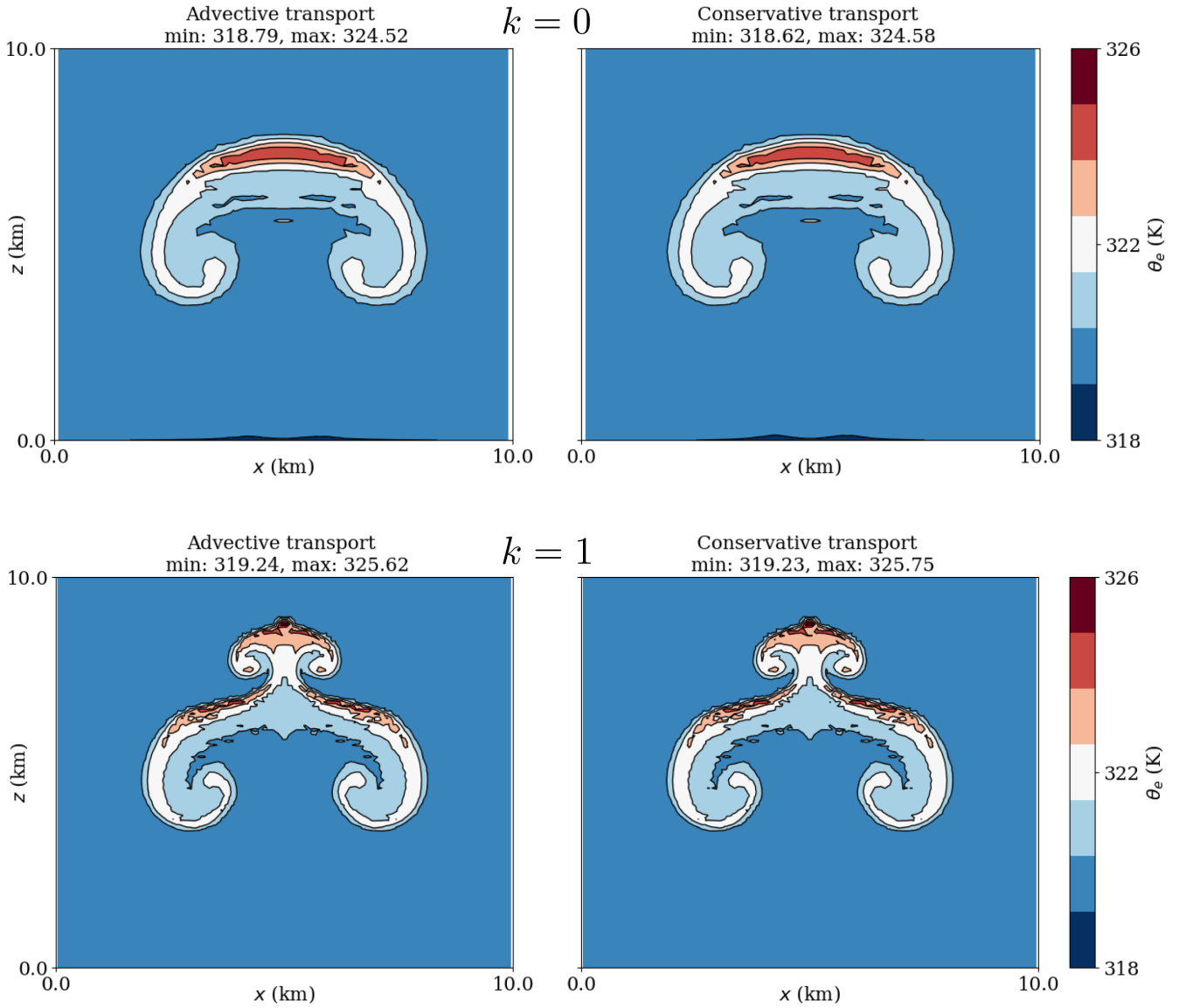


Figure 10: Plots of the wet equivalent potential temperature (θ_e) at the end of the Bryan-Fritsch moist rising bubble simulations. The top row shows the fields using lowest-order elements, and the bottom row shows next-to-lowest-order elements. For both element orders, the resulting fields are visually indistinguishable when using the advective or conservative tracer transport schemes.

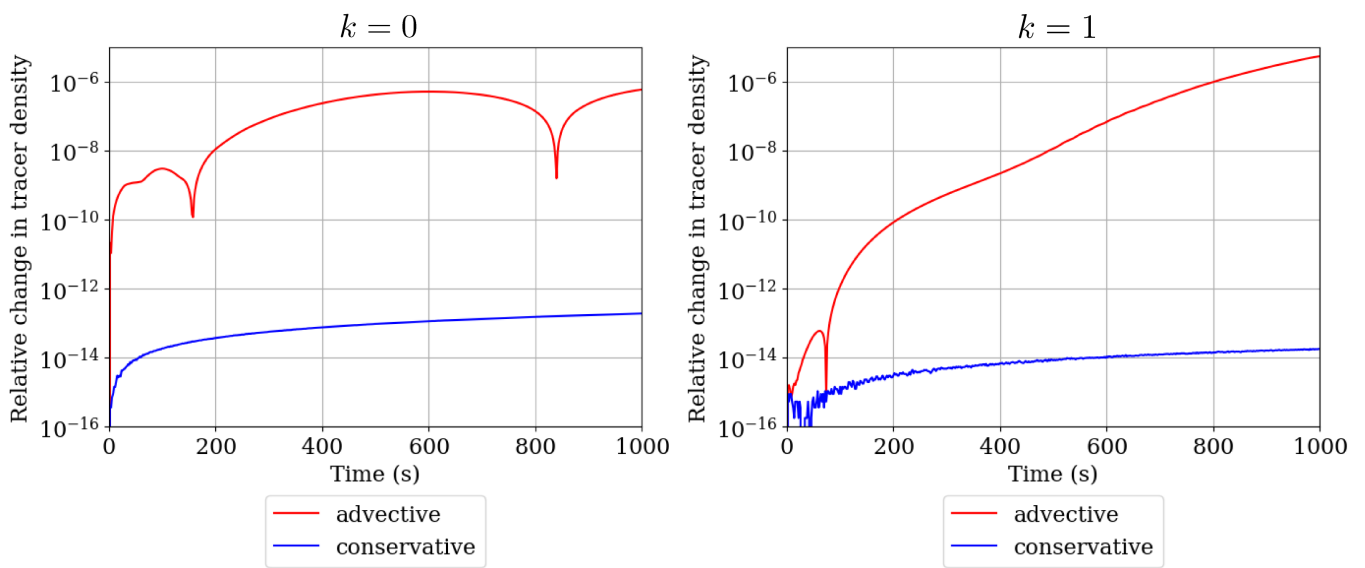


Figure 11: Relative change in tracer density (total water) over time for the Bryan-Fritsch moist rising bubble test. Lowest-order elements are shown on the left and next-to-lowest-order on the right. For both element orders, the mass conservation of the conservative tracer scheme is much better than that of the advective scheme.

7 Conclusions

This paper presented a conservative, discontinuous Galerkin, tracer transport scheme within a compatible finite element discretisation. A key feature of the method is its ability to work with a mixing ratio that is either co-located or vertically staggered from the dry density. Recovery, injection, and Galerkin projection operations are used to move fields into a shared function space for transport. To ensure mass conservation when mapping a mixing ratio, we introduce conservative recovery, conservative injection, and conservative Galerkin projection operators that act upon the tracer density of ρm . These conservative operations use three input fields: the mixing ratio and density in their original function spaces, and the density in the mapped function space.

Simulations using the Gusto code library were used to verify the desired properties of our scheme: mass conservation, consistency, and non-negativity. Mass conservation and consistency were shown in transport-only tests with co-located and vertically staggered function spaces. The use of conservative tracer transport does not degrade the rate of convergence, whilst allowing for mass conservation that is near machine precision. Consistency was shown through the preservation of spatially constant mixing ratio fields after transport. A final dynamical core-like test with the Bryan-Fritsch rising bubble showed that the conservative tracer transport can successfully conserve mass of moisture species in the compressible Euler equations when using a vertical staggering of the mixing ratios from the dry density.

The non-negativity property of the new transport scheme was addressed through a mean mixing ratio limiter, which blends a next-to-lowest-order mixing ratio with a lowest-order counterpart to ensure mass conservation is maintained. This work focused on implementing the limiter for co-located spaces, so future work will extend the limiter to function spaces that have continuity requirements in the vertical dimension. Monotonicity of the transport scheme, which is a more comprehensive property than non-negativity, would also be a desirable addition; this would enforce that the mixing ratio is bounded above by one. In the future, we would like to apply the conservative tracer transport scheme to other equation sets and configurations such as the family of moist shallow water equations from Hartney et al. (2025).

Code Availability

The GitHub repository for Gusto can be found at <https://github.com/firedrakeproject/gusto>. Python scripts for running the Gusto simulations and figure making can be found at the GitHub repository https://github.com/ta440/gusto_conservative_transport. Many of the visualisations used plotting functions from the tomplot GitHub repository <https://github.com/tommhendall/tomplot>.

Appendix A: Test case setups

A.1 Co-located transport-only test on the sphere

We use the divergent flow field described in Appendix A of Lauritzen et al. (2015). Using u to denote the zonal flow along lines of constant longitude, $\lambda \in [-\pi, \pi)$, and v the meridional flow along lines of constant latitude, $\phi \in [-\pi/2, \pi/2]$, the velocity field is

$$u(\lambda, \phi, t) = \frac{2\pi a}{\tau} \cos(\phi) - k \sin^2\left(\frac{\lambda'}{2}\right) \sin(2\phi) \cos^2(\phi) \cos\left(\frac{\pi t}{\tau}\right), \quad (33a)$$

$$v(\lambda, \phi, t) = \frac{k}{2} \sin(\lambda') \cos^3(\phi) \cos\left(\frac{\pi t}{\tau}\right), \quad (33b)$$

where $k = 5a/\tau$, $\lambda' = \lambda - 2\pi at/\tau$, and τ is the time period for the flow to return to its initial state, which is set to the simulation length of twelve days ($\tau = 1,036,800$ s). The mean flow term of $2\pi a \cos(\phi)/\tau$ in (33a) breaks the symmetry of the flow field to ensure that errors generated in the first half of the simulation are not reversed in the second half, which can lead to misleadingly small transport errors. A timestep size of $\Delta t = 450$ s is used for all tests.

The smooth scalar field option from Nair and Lauritzen (2010) is chosen to initialise the mixing ratio in the convergence test and the density in the consistency test. This defines Gaussian perturbations of

$$g_i(\lambda_i, \phi_i) = g_{\max} \exp(-b_0[(X - X_i) + (Y - Y_i) + (Z - Z_i)]), \quad (34)$$

where the Cartesian coordinates of (X, Y, Z) are computed from longitude-latitude (λ, ϕ) coordinates using

$$X = a \cos(\phi) \cos(\lambda), \quad Y = a \cos(\phi) \sin(\lambda), \quad Z = a \sin(\phi), \quad (35)$$

where $a = 6371.22$ km is taken as the Earth's radius. We select a Gaussian decay rate of $b_0 = 5$ and centre the two Gaussian bumps at $(\lambda_1, \phi_1) = (-\pi/4, 0)$ and $(\lambda_2, \phi_2) = (\pi/4, 0)$.

The convergence setting uses

$$\rho(\lambda, \phi, t = 0) = \rho_b + 0.5 \cos(\phi), \quad (36a)$$

$$m(\lambda, \phi, t = 0) = m_0 + g_1 + g_2, \quad (36b)$$

with $\rho_b = 1 \text{ kg m}^{-3}$, $m_0 = 0.02 \text{ kg kg}^{-1}$, and $g_{\max} = 0.05 \text{ kg kg}^{-1}$. Spatial resolutions of $N_e \in \{16, 24, 36, 48\}$ are used with $k = 0$ elements and $N_e \in \{8, 16, 24, 32\}$ for $k = 1$, where N_e denotes the number of cells along a cubed-sphere panel edge.

The consistency setting uses

$$\rho(\lambda, \phi, t = 0) = \rho_b + g_1 + g_2, \quad (37a)$$

$$m(\lambda, \phi, t = 0) = m_0, \quad (37b)$$

with $\rho_b = 1 \text{ kg m}^{-3}$, $m_0 = 0.02 \text{ kg kg}^{-1}$, and $g_{\max} = 0.5 \text{ kg m}^{-3}$. Spatial resolutions of $N_e = 32$ and $N_e = 48$ are used with $k = 1$ and $k = 0$ elements, respectively.

A.2 Vertically staggered transport-only test in a vertical slice

The transporting velocity of $\mathbf{u} = [u, w]^T$, with u the horizontal component of the wind and w the vertical component of the wind, is described by

$$u(x, z, t) = U - \frac{W\pi L_x}{H_z} \cos\left(\frac{\pi t}{\tau}\right) \cos\left(\frac{2\pi x'}{L_x}\right) \cos\left(\frac{\pi z}{H_z}\right), \quad (38a)$$

$$w(x, z, t) = 2\pi W \cos\left(\frac{\pi t}{\tau}\right) \sin\left(\frac{2\pi x'}{L_x}\right) \sin\left(\frac{\pi z}{H_z}\right), \quad (38b)$$

with $U = L_x/\tau$, $W = U/10$, $x' = x - Ut$. The domain is a square of length $L_x = 2000$ m and height $H_z = 2000$ m. The cells are set to a unity aspect ratio of $\Delta x = \Delta z = N/L_x$, where N is the number of elements in each dimension. Periodic boundary conditions apply in the x -coordinate, with the top and bottom boundaries enforcing an impermeability condition. The simulation time is $\tau = 2000$ s and a timestep of $\Delta t = 2$ s is used for all tests.

Gaussian perturbations are defined on the vertical slice domain as

$$f(x_c, z_c) = f_0 \exp(-l^2(x_c, z_c)/l_c^2), \quad (39)$$

with f_0 the amplitude of the perturbation, $l^2(x_c, z_c) = (\min\{|x - x_c|, L_x - |x - x_c|\})^2 + |z - z_c|^2$ the shortest squared distance from the centre of a perturbation at (x_c, z_c) , and $l_c = 2L_x/25$ the decay rate of the Gaussian functions. The Gaussian perturbations are centred at $(x_1, z_1) = (3L_x/8, H_z/2)$ and $(x_2, z_2) = (5L_x/8, H_z/2)$.

The convergence setting uses

$$\rho(x, z, t = 0) = \rho_b + (\rho_t - \rho_b) \frac{z}{H_z}, \quad (40a)$$

$$m(x, z, t = 0) = m_0 + f(x_1, z_1) + f(x_2, z_2). \quad (40b)$$

with $\rho_b = 1 \text{ kg m}^{-3}$, $\rho_t = 0.5 \text{ kg m}^{-3}$, $m_0 = 0.02 \text{ kg kg}^{-1}$, and $f_0 = 0.05 \text{ kg kg}^{-1}$. The spatial resolutions are $N \in \{50, 60, 70, 80, 90, 100\}$ for $k = 1$ and $N \in \{100, 120, 140, 160, 180, 200\}$ for $k = 0$.

The consistency setting uses

$$\rho(x, z, t = 0) = \rho_b + f(x_1, z_1) + f(x_2, z_2), \quad (41a)$$

$$m(x, z, t = 0) = m_0, \quad (41b)$$

with $\rho_b = 0.5 \text{ kg m}^{-3}$, $f_0 = 0.5 \text{ kg m}^{-3}$, and $m_0 = 0.02 \text{ kg kg}^{-1}$. The spatial resolutions are $N = 100$ for $k = 1$ and $N = 200$ for $k = 0$.

A.3 MMR limiter test

The test for the mean mixing ratio limiter is similar to the convergence configuration of the co-located transport-only test, and uses the same prescribed velocity (33) and initial density field (36a). The mixing ratio is initialised by two slotted-cylinder functions (Nair & Lauritzen, 2010),

$$m(\lambda, \phi, t = 0) = \begin{cases} 1, & \text{if } r_1 < 0.5, |\lambda - \lambda_1| > 1/12, \\ 1, & \text{if } r_2 < 0.5, |\lambda - \lambda_2| > 1/12, \\ 1, & \text{if } r_1 < 0.5, |\lambda - \lambda_1| \leq 1/12, (\theta - \theta_1) > -5/24, \\ 1, & \text{if } r_2 < 0.5, |\lambda - \lambda_1| \leq 1/12, (\theta - \theta_1) > 5/24, \\ 0, & \text{else,} \end{cases} \quad (42)$$

with the cylinders centred at $(\lambda_1, \phi_1) = (-\pi/4, 0)$ and $(\lambda_2, \phi_2) = (\pi/4, 0)$, and r_i the great arc angle of

$$r_i(\lambda, \phi) = \arccos(\sin(\phi) \sin(\phi_i) + \cos(\phi) \cos(\phi_i) \cos(\lambda - \lambda_i)). \quad (43)$$

A spatial resolution of 24 cells per panel edge and a timestep of $\Delta t = 450$ s are used.

A.4 Terminator Toy test

The reaction rates for the interaction of chemical species, k_1 and k_2 , are given by

$$k_1(\lambda, \phi) = \max\{0, \sin(\phi) \sin(\phi_c) + \cos(\phi) \cos(\phi_c) \cos(\lambda - \lambda_c)\}, \quad (44a)$$

$$k_2(\lambda, \theta) = 1, \quad (44b)$$

with $(\lambda_c, \phi_c) = (\pi/9, -\pi/3)$ the location of the peak reaction rate of $k_1 = 1$.

The initial molecular mass of $X_T(0) = 4 \times 10^{-6}$ is distributed between the two species by

$$X(0) = D - r, \quad X_2(0) = 0.5(X_T(0) - D + r), \quad (45)$$

where $r = k_1/4k_2$, and $D = \sqrt{r^2 + 2rX_T}$. The initial condition for the dry density is the Gaussian bumps used in the co-located consistency test (37a). The prescribed non-divergent velocity field is case-2 from Nair and Lauritzen (2010) with the addition of a zonal mean flow,

$$u(\lambda, \phi, t) = k \sin^2(\lambda') \sin(2\phi) \cos\left(\frac{\pi t}{\tau}\right) + \frac{2\pi a}{\tau} \cos(\phi), \quad (46a)$$

$$v(\lambda, \phi, t) = k \sin(2\lambda') \cos(\phi) \cos\left(\frac{\pi t}{\tau}\right), \quad (46b)$$

with $k = 10a/\tau$, $\lambda' = \lambda - 2\pi t/\tau$. The full simulation time is twelve days, i.e. $\tau = 1,036,800$ s. A spatial resolution of 24 cells per panel edge and a timestep of $\Delta t = 450$ s are used.

A.5 Dynamical core test

The test parameters and initial condition follow those in Bendall et al. (2020), which is a vertical slice modification of the rising bubble test from Bryan and Fritsch (2002). The domain is of length $L_x = 10$ km and height $H_z = 10$ km. Fifty elements are used along both the length and the height dimensions, so $\Delta x = \Delta z = 200$ m. Tests with both lowest and next-to-lowest-order elements use a timestep size of $\Delta t = 2$ s and a simulation length of 1000 s.

As noted in Bendall et al. (2023), the constant mixing ratio initialisation of Bryan and Fritsch (2002) can lead to surprisingly good conservation with advective form transport; this is due to a cancellation of individual conservation errors in the cloud water and water vapour fields in the tracer density of $\rho_X = \rho(m_v + m_c)$. This fortuitous mass conservation with advective transport was indeed observed in initial tests. To avoid this, the initial mixing ratio is defined to linearly vary in the vertical coordinate,

$$m(x, z, t = 0) = m_0 - \frac{z\Delta m}{H_z}, \quad (47)$$

with $m_0 = 0.02$ kg kg⁻¹, $\Delta m = 0.005$ kg kg⁻¹. The initial water vapour is set to a saturation value, with the cloud water comprising the remainder of the initial mixing ratio. A perturbation is applied to the initial θ_{vd} field.

A novel feature of the SIQN method in Gusto, compared to GungHo, is the ability to use different explicit timesteppers for the transport of each field in the outer loop. We use the implicit midpoint rule for the transport of \mathbf{u} when $k = 1$ and SSPRK3 when $k = 0$, and SSPRK3 with both element orders for the other fields ($\rho, \theta_{vd}, m_v, m_c$). The transport term in the momentum equation (29a) is solved with the advective form of $(\mathbf{u} \cdot \nabla)\mathbf{u}$ for lowest-order elements, but is replaced by the vector-invariant form of $(\nabla \times \mathbf{u}) \times \mathbf{u} + \frac{1}{2}|\nabla \mathbf{u}|^2$ when $k = 1$. In each iteration of the SIQN outer loop, an advecting velocity is first identified, then used to transport each field. The transport of each field is typically performed separately in Gusto, but this was modified to allow ρ, m_v , and m_c to be transported simultaneously in the conservative tracer scheme.

References

Adams, S. V., Ford, R. W., Hambley, M., Hobson, J., Kavčič, I., Maynard, C. M., Melvin, T., Müller, E. H., Mullerworth, S., Porter, A. R., et al. (2019). LFRic: Meeting the challenges of scalability and performance portability in weather and climate models. *Journal of Parallel and Distributed Computing*, 132, 383–396.

- Balay, S., Abhyankar, S., Adams, M., Brown, J., Brune, P., Buschelman, K., Constantinescu, E., Dener, A., Faibussowitsch, J., Gropp, W., et al. (2024). *PETSc/TAO users manual revision 3.22* (tech. rep.). Argonne National Laboratory (ANL), Argonne, IL (United States).
- Balay, S., Gropp, W. D., McInnes, L. C., & Smith, B. F. (1997). Efficient management of parallelism in object-oriented numerical software libraries. In *Modern software tools for scientific computing* (pp. 163–202). Springer.
- Bendall, T. M., Cotter, C. J., & Shipton, J. (2019). The ‘recovered space’ advection scheme for lowest-order compatible finite element methods. *Journal of Computational Physics*, *390*, 342–358.
- Bendall, T. M., Gibson, T. H., Shipton, J., Cotter, C. J., & Shipway, B. (2020). A compatible finite-element discretisation for the moist compressible Euler equations. *Quarterly Journal of the Royal Meteorological Society*, *146*(732), 3187–3205.
- Bendall, T. M., & Kent, J. (2025). SWIFT: A monotonic, flux-form semi-Lagrangian tracer transport scheme for flow with large Courant numbers. *Monthly Weather Review*.
- Bendall, T. M., Wood, N., Thuburn, J., & Cotter, C. J. (2023). A solution to the trilemma of the moist Charney–Phillips staggering. *Quarterly Journal of the Royal Meteorological Society*, *149*(750), 262–276.
- Bendall, T. M. (2019). *On coupling resolved and unresolved physical processes in finite element discretisations of geophysical fluids* [Doctoral dissertation, Imperial College London].
- Bosler, P. A., Bradley, A. M., & Taylor, M. A. (2019). Conservative multimoment transport along characteristics for discontinuous Galerkin methods. *SIAM Journal on Scientific Computing*, *41*(4), B870–B902.
- Brown, A., Bendall, T. M., Boutle, I., Melvin, T., & Shipway, B. (2024). Physics–dynamics–chemistry coupling across different meshes in LFRic-Atmosphere: Formulation and idealised tests. *Quarterly Journal of the Royal Meteorological Society*, *150*(764), 4650–4670.
- Bryan, G. H., & Fritsch, J. M. (2002). A benchmark simulation for moist nonhydrostatic numerical models. *Monthly Weather Review*, *130*(12), 2917–2928.
- Cockburn, B., & Shu, C.-W. (2001). Runge–Kutta discontinuous Galerkin methods for convection-dominated problems. *Journal of scientific computing*, *16*, 173–261.
- Cotter, C. J. (2023). Compatible finite element methods for geophysical fluid dynamics. *Acta Numerica*, *32*, 291–393.
- Cotter, C. J., & Kuzmin, D. (2016). Embedded discontinuous Galerkin transport schemes with localised limiters. *Journal of Computational Physics*, *311*, 363–373.
- Cotter, C. J., & Shipton, J. (2012). Mixed finite elements for numerical weather prediction. *Journal of Computational Physics*, *231*(21), 7076–7091.
- Durrant, D. R. (2010). *Numerical methods for fluid dynamics: With applications to geophysics* (Vol. 32). Springer Science & Business Media.
- Durrant, D. R., & Klemp, J. B. (1982). On the effects of moisture on the Brunt–Väisälä frequency. *Journal of the Atmospheric Sciences*, *39*(10), 2152–2158.
- Georgoulis, E. H., & Pryer, T. (2018). Recovered finite element methods. *Computer Methods in Applied Mechanics and Engineering*, *332*, 303–324.
- Gibson, T. H., McRae, A. T., Cotter, C. J., Mitchell, L., & Ham, D. A. (2019). *Compatible finite element methods for geophysical flows: Automation and implementation using Firedrake*. Springer Nature.
- Giraldo, F. X. (1997). Lagrange–Galerkin methods on spherical geodesic grids. *Journal of Computational Physics*, *136*(1), 197–213.
- Ham, D. A., Kelly, P. H. J., Mitchell, L., Cotter, C. J., Kirby, R. C., Sagiya, K., Bouziani, N., Vorderwuelbecke, S., Gregory, T. J., Betteridge, J., Shapero, D. R., Nixon-Hill, R. W., Ward, C. J., Farrell, P. E., Brubeck, P. D., Marsden, I., Gibson, T. H., Homolya, M., Sun, T., . . . Markall, G. R. (2023, May). *Firedrake user manual* (First edition). Imperial College London, University of Oxford, Baylor University, and University of Washington. <https://doi.org/10.25561/104839>

- Hartney, N., Bendall, T. M., & Shipton, J. (2025). Exploring forms of the moist shallow-water equations using a new compatible finite-element discretisation. *Quarterly Journal of the Royal Meteorological Society*, e70018.
- Herrington, A. R., Lauritzen, P. H., Reed, K. A., Goldhaber, S., & Eaton, B. E. (2019). Exploring a lower-resolution physics grid in CAM-SE-CSLAM. *Journal of Advances in Modeling Earth Systems*, 11(7), 1894–1916.
- Kuzmin, D. (2010). A vertex-based hierarchical slope limiter for p-adaptive discontinuous Galerkin methods. *Journal of Computational and Applied Mathematics*, 233(12), 3077–3085.
- Lauritzen, P. H., Nair, R. D., & Ullrich, P. A. (2010). A conservative semi-Lagrangian multi-tracer transport scheme (CSLAM) on the cubed-sphere grid. *Journal of Computational Physics*, 229(5), 1401–1424.
- Lauritzen, P., Conley, A., Lamarque, J.-F., Vitt, F., & Taylor, M. (2015). The terminator “toy” chemistry test: A simple tool to assess errors in transport schemes. *Geoscientific Model Development*, 8(5), 1299–1313.
- Machenhauer, B., Kaas, E., & Lauritzen, P. H. (2009). Finite-volume methods in meteorology. In *Handbook of numerical analysis* (pp. 3–120, Vol. 14). Elsevier.
- Melvin, T., Benacchio, T., Shipway, B., Wood, N., Thuburn, J., & Cotter, C. (2019). A mixed finite-element, finite-volume, semi-implicit discretization for atmospheric dynamics: Cartesian geometry. *Quarterly Journal of the Royal Meteorological Society*, 145(724), 2835–2853.
- Melvin, T., Benacchio, T., Thuburn, J., & Cotter, C. (2018). Choice of function spaces for thermodynamic variables in mixed finite-element methods. *Quarterly Journal of the Royal Meteorological Society*, 144(712), 900–916.
- Melvin, T., Shipway, B., Wood, N., Benacchio, T., Bendall, T., Boutle, I., Brown, A., Johnson, C., Kent, J., Pring, S., et al. (2024). A mixed finite-element, finite-volume, semi-implicit discretisation for atmospheric dynamics: Spherical geometry. *Quarterly Journal of the Royal Meteorological Society*.
- Nair, R. D., & Lauritzen, P. H. (2010). A class of deformational flow test cases for linear transport problems on the sphere. *Journal of Computational Physics*, 229(23), 8868–8887.
- Nair, R. D., Levy, M. N., & Lauritzen, P. H. (2011). Emerging numerical methods for atmospheric modeling. In *Numerical Techniques for Global Atmospheric Models* (pp. 251–311). Springer.
- Nair, R. D., Thomas, S. J., & Loft, R. D. (2005). A discontinuous Galerkin transport scheme on the cubed sphere. *Monthly Weather Review*, 133(4), 814–828.
- Natale, A., Shipton, J., & Cotter, C. J. (2016). Compatible finite element spaces for geophysical fluid dynamics. *Dynamics and Statistics of the Climate System*, 1(1), 1–31.
- Ronchi, C., Iacono, R., & Paolucci, P. S. (1996). The “cubed sphere”: A new method for the solution of partial differential equations in spherical geometry. *Journal of Computational Physics*, 124(1), 93–114.
- Satoh, M., Matsuno, T., Tomita, H., Miura, H., Nasuno, T., & Iga, S.-I. (2008). Nonhydrostatic icosahedral atmospheric model (NICAM) for global cloud resolving simulations. *Journal of Computational Physics*, 227(7), 3486–3514.
- Shu, C.-W., & Osher, S. (1988). Efficient implementation of essentially non-oscillatory shock-capturing schemes. *Journal of computational physics*, 77(2), 439–471.
- Skamarock, W. C., Klemp, J. B., Duda, M. G., Fowler, L. D., Park, S.-H., & Ringler, T. D. (2012). A multiscale nonhydrostatic atmospheric model using centroidal Voronoi tessellations and C-grid staggering. *Monthly Weather Review*, 140(9), 3090–3105.
- Staniforth, A., & Thuburn, J. (2012). Horizontal grids for global weather and climate prediction models: A review. *Quarterly Journal of the Royal Meteorological Society*, 138(662), 1–26.
- Thuburn, J. (2008). Some conservation issues for the dynamical cores of NWP and climate models. *Journal of Computational Physics*, 227(7), 3715–3730.
- Wood, N., Staniforth, A., White, A., Allen, T., Diamantakis, M., Gross, M., Melvin, T., Smith, C., Vosper, S., Zerroukat, M., et al. (2014). An inherently mass-conserving semi-implicit semi-

- Lagrangian discretization of the deep-atmosphere global non-hydrostatic equations. *Quarterly Journal of the Royal Meteorological Society*, 140(682), 1505–1520.
- Zerroukat, M., Wood, N., & Staniforth, A. (2002). SLICE: A Semi-Lagrangian Inherently Conserving and Efficient scheme for transport problems. *Quarterly Journal of the Royal Meteorological Society*, 128(586), 2801–2820.
- Zhang, K., Wan, H., Wang, B., & Zhang, M. (2008). Consistency problem with tracer advection in the atmospheric model GAMIL. *Advances in Atmospheric Sciences*, 25, 306–318.